LUND UNIVERSITY

Advanced Vascular Imaging. From Wall to Plaque.

Truong, My

2021

Document Version:
Publisher's PDF, also known as Version of record

[Link to publication](#)

Citation for published version (APA):
Truong, M. (2021). *Advanced Vascular Imaging. From Wall to Plaque.* Lund University, Faculty of Medicine.

Total number of authors:
1

Advanced Vascular Imaging

From Wall to Plaque

MY TRUONG

DEPARTMENT OF CLINICAL SCIENCES | LUND UNIVERSITY

Advanced Vascular Imaging

From Wall to Plaque

My Truong M.D

Department of Diagnostic Radiology

Department of Clinical Sciences

LUND
UNIVERSITY

Organization	Document name
LUND UNIVERSITY Faculty of Medicin Department of Clinical Sciences Department of Diagnostic Radiology	DOCTORAL DISSERTATION
Author My Truong	**Date of issue** June 10th, 2021

Title and subtitle
Advanced vascular imaging - from wall to plaque

Abstract

Background: Stroke is a major cause of disability worldwide. A common cause of stroke is arterial wall changes due to atherosclerosis in the carotid bifurcation and intracranial arteries. Diagnosis and understanding of arterial wall pathologies rely on radiologic imaging as well as histology. Clinical imaging, such as ultrasonography, CTA, and MRI, are validated with histology, but the differences in image characteristics and resolution between radiology and histology can make comparison challenging.

Aim: Using advanced imaging methods to study the carotid and intracranial arterial wall and the atherosclerotic plaque in high-resolution MRI and CT, *in vivo* and *ex vivo*.

Methods: In paper **I**, 3T vessel wall MRI of the carotid arterial bifurcation was performed on 34 stroke and TIA patients. We used a T1w and a T2*w SPGR sequence to detect elevated T1w signal and susceptibility effects in non-calcified plaque components, previously seen on CTA. We scanned 12 resected carotid plaques in paper **II** in 11.7T MRI with T1 and T2* maps. The histologic sections from corresponding plaque levels were used to categorize ROI data and classify plaque components with quadratic discriminant analysis. In paper **III**, we scanned the middle cerebral arteries in patients within 48h after thrombectomy in 7T MRI with motion correction and compared vessel wall contrast enhancement on the symptomatic side with the untreated side. We scanned five plaques with synchrotron-radiation-based micro-CT with submicron voxel size and compared them with histology in paper **IV**.

Results: In paper **I**, we found that a third of all areas in non-calcified plaque components showed susceptibility effects with no co-localization of elevated T1w signal, indicating the possibility of hemosiderin or micro-calcification content. In paper **II**, we showed that *ex vivo* high field quantitative MRI is a promising method to classify plaque components such as lipids and fibrous tissue. In contrast, hemorrhage and areas of inflammation were more challenging to classify. In paper **III**, we showed that contrast enhancement in the arterial wall after thrombectomy was found in segments corresponding to stent-retriever deployment and expansion. In paper **IV**, we showed that synchrotron-based micro-CT renders images with submicron voxel size, making the micro-structures of plaque-typical morphology visually comparable with histology.

Conclusion: Advanced vascular imaging with high resolution and high contrast enhance the three-dimensional understanding of the vessel wall and the atherosclerotic plaque morphology, potentially facilitating comparison between radiology and histology.

Keywords: atherosclerosis, vessel wall, carotid, stroke, high field MRI, synchrotron μCT, 3T & 7T MRI

Classification system and index terms (if any)

Supplementary bibliographical information		**Language** English
ISSN and key title 1652-8220		**ISBN** 978-91-8021-067-6
Recipient's notes	**Number of pages** 77	Price
	Security classification	

Signature   Lund 2021-05-04

Advanced vascular imaging

From wall to plaque

My Truong M.D

To my family

Table of Contents

Original papers

This thesis is based on the following papers, referenced in the text by their Roman numerals. The complete papers are appended at the end of the printed thesis. Paper II and III are reprinted in accordance with open access licenses.

I. **My Truong**, Claes Håkansson, Makda HaileMichael, Jonas Svensson, Jimmy Lätt, Karin Markenroth Bloch, Roger Siemund, Isabel Goncalves and Johan Wasselius. *The potential role of T2*-weighted multi-echo data image combination as an imaging marker for intraplaque hemorrhage in carotid plaque imaging.* (Unpublished manuscript, submitted)

II. **My Truong**, Finn Lennartsson, Adnan Bibic, Lena Sundius, Ana Persson, Roger Siemund, René In't Zandt, Isabel Goncalves, Johan Wasselius. *Classifications of atherosclerotic plaque components with T1 and T2* mapping in 11.7T MR.* European Journal of Radiology Open, 8(2021), 100323

III. **My Truong**, Karin Markenroth Bloch, Mads Andersen, Gunnar Andsberg, Johannes Töger and Johan Wasselius. *Subacute vessel wall imaging at 7T MRI in post-thrombectomy stroke patients*. Neuroradiology 2019; 61(10): 1145–1153

IV. **My Truong*,** Till Dreier*, Johan Wasselius, Lena Sundius, Ana Persson, Goran Lovric, Anne Bonnin, Isabel Goncalves and Martin Bech. *Sub-micrometer morphology of human atherosclerotic plaque revealed by synchrotron radiation-based µCT - a comparison with histology*. (Unpublished manuscript, submitted)

* Both authors contributed equally to the paper.

Abstract

Title: Advanced vascular imaging - from wall to plaque.

Background: Stroke is a major cause of disability worldwide. A common cause of stroke is arterial wall changes due to atherosclerosis in the carotid bifurcation and intracranial arteries. Diagnosis and understanding of arterial wall pathologies rely on radiologic imaging as well as histology. Clinical imaging, such as ultrasonography, CTA, and MRI, are validated with histology, but the differences in image characteristics and resolution between radiology and histology can make comparison challenging.

Aim: Using advanced imaging methods to study the carotid and intracranial arterial wall and the atherosclerotic plaque in high-resolution MRI and CT, *in vivo* and *ex vivo*.

Methods: In paper **I**, 3T vessel wall MRI of the carotid arterial bifurcation was performed on 34 stroke and TIA patients. We used a T1w and a T2*w SPGR sequence to detect elevated T1w signal and susceptibility effects in non-calcified plaque components, previously seen on CTA. We scanned 12 resected carotid plaques in paper **II** in 11.7T MRI with T1 and T2* maps. The histologic sections from corresponding plaque levels were used to categorize ROI data and classify plaque components with quadratic discriminant analysis. In paper **III**, we scanned the middle cerebral arteries in patients within 48h after thrombectomy in 7T MRI with motion correction and compared vessel wall contrast enhancement on the symptomatic side with the untreated side. We scanned five plaques with synchrotron-radiation-based micro-CT with submicron voxel size and compared them with histology in paper **IV**.

Results: In paper **I**, we found that a third of all areas in non-calcified plaque components showed susceptibility effects with no co-localization of elevated T1w signal, indicating the possibility of hemosiderin or micro-calcification content. In paper **II**, we showed that *ex vivo* high field quantitative MRI is a promising method to classify plaque components such as lipids and fibrous tissue. In contrast, hemorrhage and areas of inflammation were more challenging to classify. In paper **III**, we showed that contrast enhancement in the arterial wall after thrombectomy was found in segments corresponding to stent-retriever deployment and expansion. In paper **IV**, we showed that synchrotron-based micro-CT renders images with submicron voxel size, making the micro-structures of plaque-typical morphology visually comparable with histology.

Conclusion: Advanced vascular imaging with high resolution and high contrast enhance the three-dimensional understanding of the vessel wall and the atherosclerotic plaque morphology, potentially facilitating comparison between radiology and histology.

Abbreviations

AIS	Acute ischemic stroke
Al	Aluminum
CEA	Carotid endarterectomy
CI	Confidence interval
CPIP	Carotid plaque imaging project
CPU	Central processing unit
CT	Computed tomography
CTA	Computed tomography angiography.
DSA	Digital subtraction angiography
DUS	Duplex ultrasonography
ECA	External carotid artery
Fe	Ferrum (Iron)
FA	Flip angle
GB	Gigabyte
Gd	Gadolinium
HU	Hounsfield unit
HR	High resolution
ICA	Internal carotid artery
iMOCO	interleaved prospective motion correction.
IPH	Intra plaque hemorrhage
IQR	Interquartile range
keV	Kiloelectron volt
LR	Low resolution
LRNC	Lipid rich necrotic core
LBIC	Lund BioImaging Center
MAX IV	Microtron Accelerator for X-rays (IV)
MEDIC	Multi-Echo Data Image combination
MIP	Maximal intensity projection
MPIR-TSE	Magnetization Prepared Inversion Recovery-Turbo Spin Echo
MPR	Multiplanar reconstruction
MRI	Magnetic resonance imaging
M1&M2	1st and 2nd segment of the middle cerebral artery.
μCT	Micro-computed tomography
μm	Micrometer
NIHSS	National Institute of Health Stroke Score
PACS	Picture Archiving and Communication System
PSI	Paul Scherrer institute
QDA	quadratic discriminant analysis
RAM	Random access memory
ROI	Region of interest
SCAPIS	Swedish CArdioPulmonary bioImage Study

sCMOS	Scientific complementary metaloxide semiconductor
SD	Standard deviation
SSD	solid-state hard disk
SLS	Swiss light source
SNR	Signal to noise ratio
SRμCT	Synchrotron radiation-based (phase-contrast) micro-computed tomography
T	Tesla
TIA	Transient ischemic attack
TB	Terra byte
TE	Echo time
TICI	Thrombolysis in cerebral infarction
TIFF	Tagged image file format.
TOF	Time of flight
TOMCAT	TOmographic Microscopy and Coherent rAdiology experimenTs.
TR	Repetition time
T1wBB	T1 weighted black blood.
11.7T	11.7 Tesla
2D	Two-dimensional
3D	Three-dimensional

Thesis Context and Rationale

When I started my research in vessel wall imaging in 2014, vessel wall MRI with dedicated surface coils was not used in Lund. Accumulating research had shown that carotid plaque morphology visualized with MRI was emerging as an important factor in risk stratification in patients with a transient ischemic attack (TIA) and stroke(1-17). Carotid plaques and stenosis were already imaged with duplex ultrasonography and computed tomography angiography (CTA) (18, 19), both inferior in contrast resolution to MRI.

The high contrast resolution in vessel wall MRI allows us to detect plaque morphology that could indicate an advanced and vulnerable plaque. Characteristics such as intraplaque hemorrhage (IPH), large lipid-rich necrotic core (LRNC), and a thin or disrupted fibrous cap (3, 4, 13, 15, 20) indicate plaque vulnerability and has been associated with a higher risk of stroke(9, 10, 21, 22).

Our goal was to set up a state-of-the-art protocol for carotid vessel wall imaging. Additionally, we hoped to study new sequences. In collaboration with Professor Isabel Goncalves that provided us with a dedicated carotid surface coil, a protocol for carotid vessel wall MRI was set up on one of the clinic's 3T MRI cameras. We collected the data for paper I with this protocol and participated in the carotid MRI sub-study of a multicenter national research project called the Swedish CArdioPulmonary bioImage Study (SCAPIS).

In collaboration with Isabel Goncalves's research group and René In't Zandt and Adnan Bibic at Lund BioImaging Center (LBIC), we also studied carotid plaques after endarterectomy in 11.7T MRI. The original plan included plaques from patients who had undergone a 3T MRI to compare *in vivo* findings from the 3T camera with *ex vivo* findings from the 11.7T camera. But the study plan was changed since most patients that were examined with carotid MRI were not eligible for endarterectomy. Instead, we focused on studying plaques from the Carotid Plaque Imaging Project (CPIP) biobank in 11.7T MRI. The plaques were scanned with T1 and T2* maps and high-resolution T1w and T2*w MRI. The scans were validated with histology, and plaque components were classified using quadratic discriminant analysis on ROI data(23), resulting in paper II.

For paper III, we decided to perform vessel wall imaging of intracranial vessels in 7T MRI. The modality offered shorter scan times and a higher signal-to-noise ratio (SNR) than 3T MRI(24-27). We hoped to establish a state-of-the-art protocol for future clinical applications in other patient groups that could develop brain ischemia, such as vasculitis or Moya moya. We also wanted to study if thrombectomy would affect the vessel wall or if the lodged thrombus was affecting the wall. During one of the 7T MRI annual workshops, I met Mads Andersen, who worked with prospective motion correction, and asked him to include the method in our study.

Due to the results in paper II, we were curious about the possibility of studying the plaques with µCT at the MAX IV facility in Lund and started to look for collaborators. Through a previous colleague to Johan Wasselius, we were referred to Martin Bech at the Department of Medical Radiation Physics at Lund University, who informed us that µCT was still on the planning level at MAX IV. It was instead possible to scan the plaques at the Swiss light source (SLS) synchrotron at the Paul Scherrer Institute (PSI). We were offered the opportunity to do a test scan, and together with Isabel Goncalves, we decided to send a plaque to PSI. The test scan showed interesting images and prompted us to start a new project in collaboration with Martin Bech's research group, René In't Zandt at LBIC, and Isabel Goncalves's research group. The original idea was to compare µMRI images with µCT and histology to detect additional tissue characteristics with non-destructive whole plaque imaging. The final data size turned out to be extensive and challenging to fit into one single paper. We decided to first compare the µCT data with histology, which resulted in paper IV.

This thesis has slowly moved from *in vivo* state-of-the-art vessel wall imaging to experimental highly specialized *ex vivo* imaging. We used *ex vivo* plaque imaging applications to make the resolution gap between clinical imaging and histology smaller and better understand clinical imaging findings. Even though the methods are diverse, the question that propelled my Ph.D. and led me from a 3T MRI camera in Lund to a synchrotron in Switzerland was always a quest to understand clinical CTA and MRI findings based on histological knowledge. As a radiologist, the method of choice was to find the matching and corresponding images between different methods and thus make them as comparable as possible.

Background

The healthy intracranial and extracranial artery

Arteries supply oxygenated blood and nutrients to the body. Healthy arteries consist of three tissue layers; the tunica intima, the tunica media, and the tunica externa that together must maintain a mechanical, immunological, and biochemical balance to function correctly(28) (Fig. 1).

Elastic laminae separate the different layers of the arterial wall. The tunica intima consists of a single layer of endothelial cells that rest on a basement membrane covering the subendothelial space(28). Tunica intima is the innermost layer and has contact with the bloodstream.

The middle layer, tunica media, consists of multiple layers of smooth muscle cells covered by another basement membrane. The tunica media is very elastic and can adapt to the pulsatile mechanical tensions caused by the difference of wall pressure between systole and diastole(28).

The outermost layer, the tunica externa (also called the adventitia), consists of connective tissue and tiny vessels called vasa vasorum, which supply the arterial wall with oxygenated blood and nutrients(28).

Intracranial arteries differ from extracranial arteries such as the carotid arteries. In intracranial arteries, the endothelial cells are joined with tight junctions and have no fenestration. Additionally, the muscle layer and the tunica externa in intracranial arteries are thinner, and the external elastic lamina is lacking (29). The tunica externa of the carotid arteries is surrounded by fatty tissue, establishing more support. In contrast, the tunica externa of intracranial arteries is surrounded by cerebrospinal fluid, with less support. (28, 29)
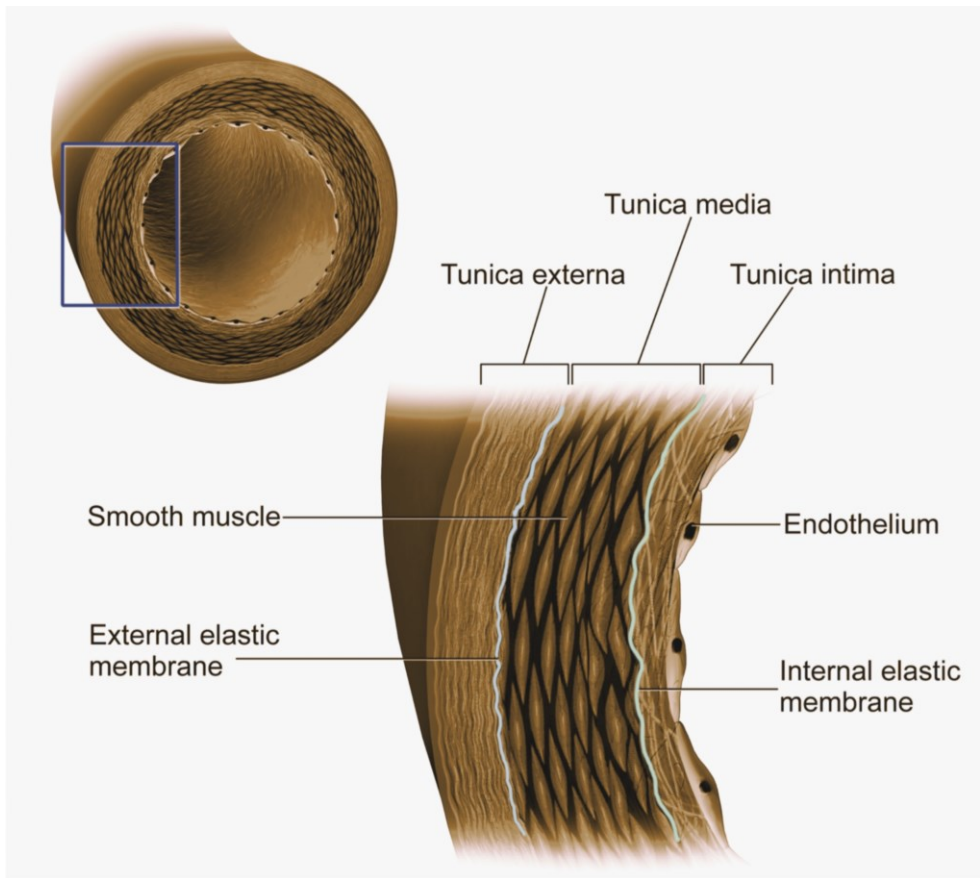
Figure 1.
Illustration of a healthy artery in cross-section. Courtesy of Blausen.com staff. CC BY 3.0. Adapted by My Truong
https://en.wikipedia.org/wiki/Artery#/media/File:Blausen_0055_ArteryWallStructure.png

Atherosclerosis

The word "atherosclerosis" is derived from the two Greek words "athera" (gruel) and "sclerosis" (hardening)(30), a descriptive name of a disease that affects medium and large arteries(28). Atherosclerosis is a systematic, chronic, and progressive disease in the vessel wall that disrupts the mechanical, immunological, and chemical balance in the vessel and lowers the function of the arteries, making them hard and rigid(31).

Stroke is the third most common cause of death worldwide (32-35). Approximately 15% of all strokes are due to atherosclerosis in large arteries, and 8% of all stroke is caused by atherosclerosis in the carotid arteries (Fig.3)(32, 36). Carotid atherosclerosis is also an indicator of cardiovascular disease in other parts of the body, such as the heart and kidneys (37-39).

Although the exact mechanisms of the initiation and development of atherosclerosis are not fully known, the result is an alteration of the wall composition and the development of an altered function. There is an accumulation of lipids, inflammatory cells, dead tissue, calcium, excessive and altered extracellular matrix, as well as neo-vascularization resulting in a general intimal thickening leading to the build-up of an atheromatous plaque that may lead to a narrowing of the lumen, intraplaque hemorrhage, or plaque rupture (Fig. 2)(31).

The disease does not affect all arteries evenly, and generally, areas with turbulent blood flow and low shear stress in medium-sized and large arteries are affected. A typical localization for forming an atheromatous plaque is in the carotid arterial bifurcation, the main vessels for the anterior cerebral blood supply.(31)
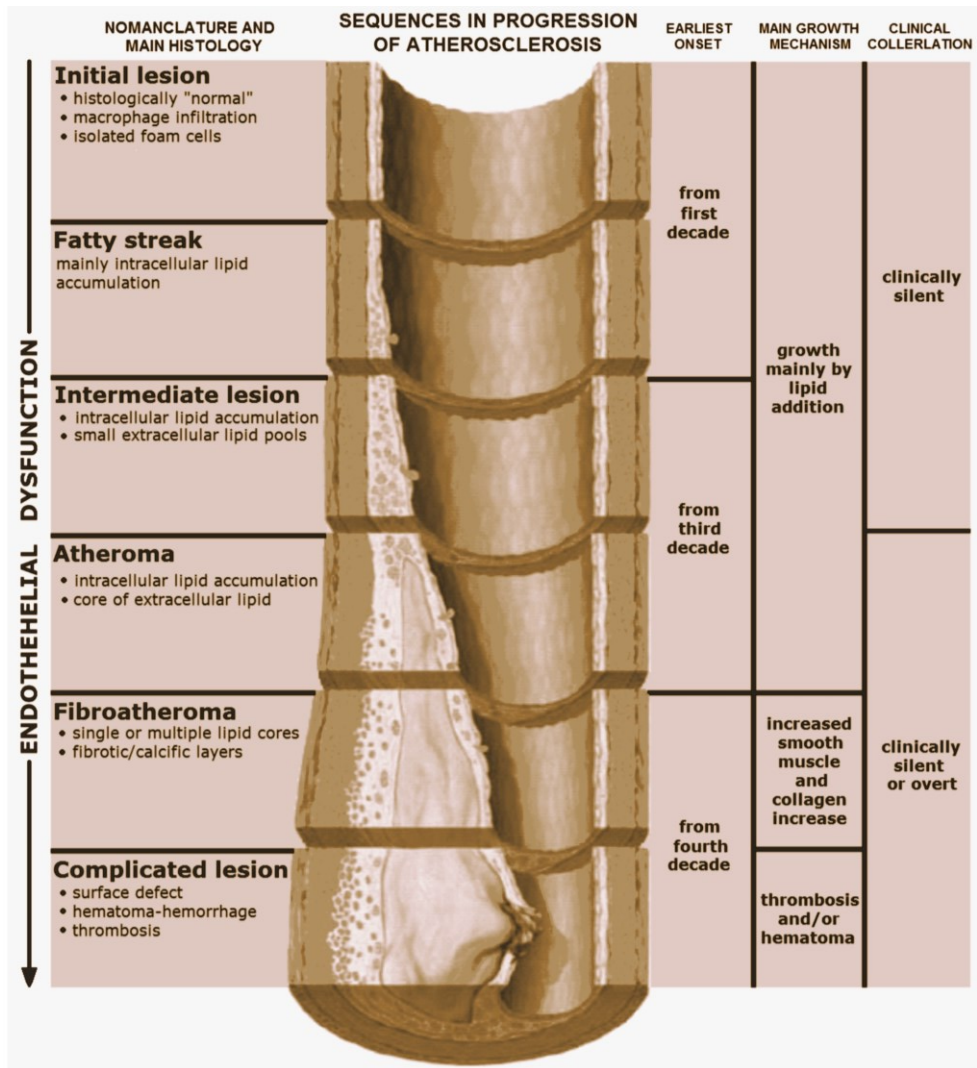
Figure 2. Illustration of progression of atherosclerosis.
Courtesy of Wikipedia Commons. CC BY 3.0. Adapted by My Truong
https://en.wikipedia.org/wiki/Atherosclerosis#/media/File:Endo_dysfunction_Athero.PNG
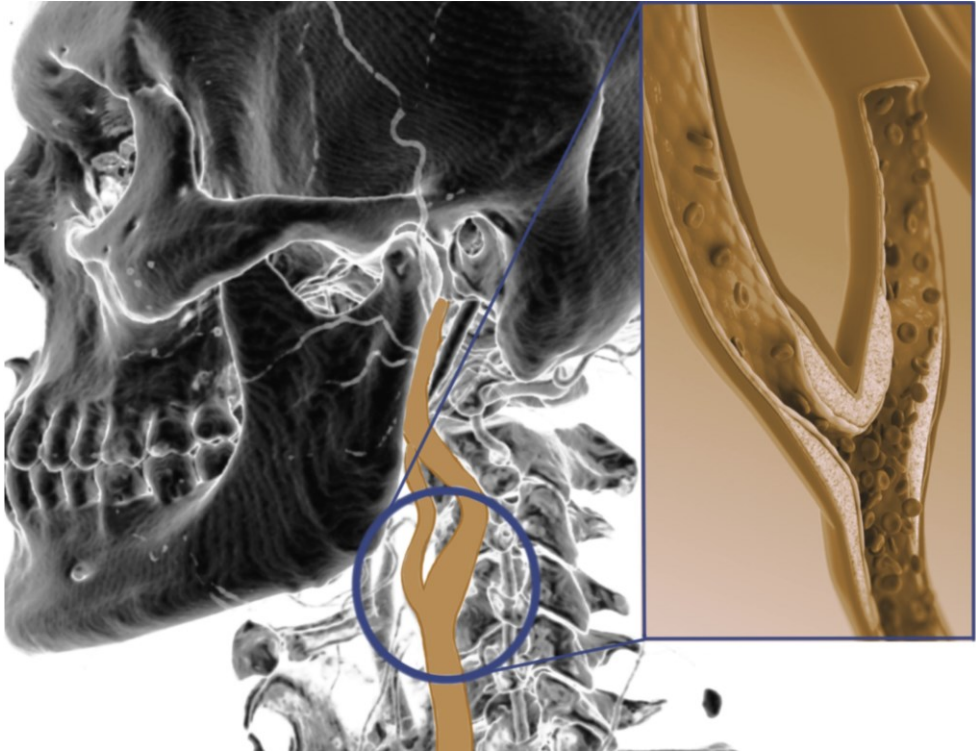
Figure 3 Atheromatous plaque at carotid bifurcation.
By My Truong. Courtesy of Scientificanimations.com for inset figure. https://www.scientificanimations.com/wiki-images/ CC 3.0.

Vessel wall on *in vivo* MRI

MRI studies of the arterial wall are mostly performed on 1,5 or 3T systems(1-5, 7, 40, 41). During the recent two decades, multiple studies have shown the feasibility of imaging plaques with inflammation, intraplaque hemorrhage, lipid-rich necrotic cores, and ruptures(1-5, 7, 15, 40-45). The method can also detect calcifications and rupture-related thrombus (2, 4, 13). Studies show a correlation between intraplaque hemorrhage and TIA and stroke (1, 7, 41, 45-47). A recent follow-up study of healthy subjects with incidental findings of IPH in the carotid bifurcation (shown with MRI) runs a higher risk of future stroke (48).

High-resolution vessel wall imaging of the carotids requires a dedicated surface coil placed on the level of the carotid bifurcation(49).

Vessel wall imaging in 7T has higher SNR and shorter scan times than 1,5 and 3T systems, making it suitable for high-resolution vascular imaging. (24, 26, 27, 49-52)

µMRI

The procedure to excise a carotid plaque is called endarterectomy. The excised plaque can be further studied with µMRI with high field strength, such as in an 11.7T system. This method allows full plaque volume scans without any prior sectioning, and the resulting image stacks can be studied in multiplanar reconstruction (MPR) and 3D. (25, 53, 54), which facilitates comparison with histology.

Ex vivo imaging with high field strengths also allows for very long scan times, providing a highly detailed visualization. The method also makes it possible for multiple rescans where different parameters can be adjusted. This method offers isotropic images with 10-50-micron resolution (55, 56), compared to *in vivo* scans at 1.5-3T, which typically allows millimeter to submillimeter resolution(57, 58).

Furthermore, µMRI allows quantitative imaging such as T1 and T2* maps based on the T1 and T2* relaxation times for each voxel, thereby potentially linking magnetic properties to specific tissue types.

Quantitative imaging based on T1, T2, and T2* maps is well established in cardiac MRI to assess the tissue composition, such as scar tissue, edema, and fatty infiltration. Alterations in the T1, T2, T2* values can indicate morphological changes linked to cardiac failure(59, 60). In *in vivo* vessel wall imaging, quantitative MRI has also been linked to disease in the carotid arteries (61, 62).

Synchrotron light

When electrons are accelerated to high speed by a large potential difference and hit certain target materials, slow down, or change direction, electromagnetic radiation such as X-ray is generated. In clinical X-ray, CT, or laboratory-based µCT, the source of radiation is an X-ray tube(63).

When the µCT is synchrotron-based, the light source is a construction, built to produce synchrotron radiation, an exceptionally bright and coherent light. In a synchrotron, the electromagnetic radiation is created by electrons accelerated to just below the speed of light and injected into a vacuum storage ring in which they circle with constant energy in a pseudo-circular fashion. The storage ring alternates straight and curved sections with periodically installed "bending"-magnets localized

along the whole ring. The magnets steer the electrons in a circular direction, forcing them to deviate from their path at each curved section. Each time the electrons turn, they emit a continuum of very bright electromagnetic radiation, the synchrotron light. The light beam emitted is tangent to the storage ring and conveyed into the various beamlines along the ring (Fig.4). Each beamline supplies a separate lab where the experiment is conducted(63).

Synchrotron light has a very high brilliance and depending on what kind of experiment, different wave lengths from the electromagnetic spectrum can be selected with high precision(63). In synchrotron-based µCT, the X-ray beams are exceptionally parallel, and microscopic objects can be scanned with extremely high resolution and high contrast(64).
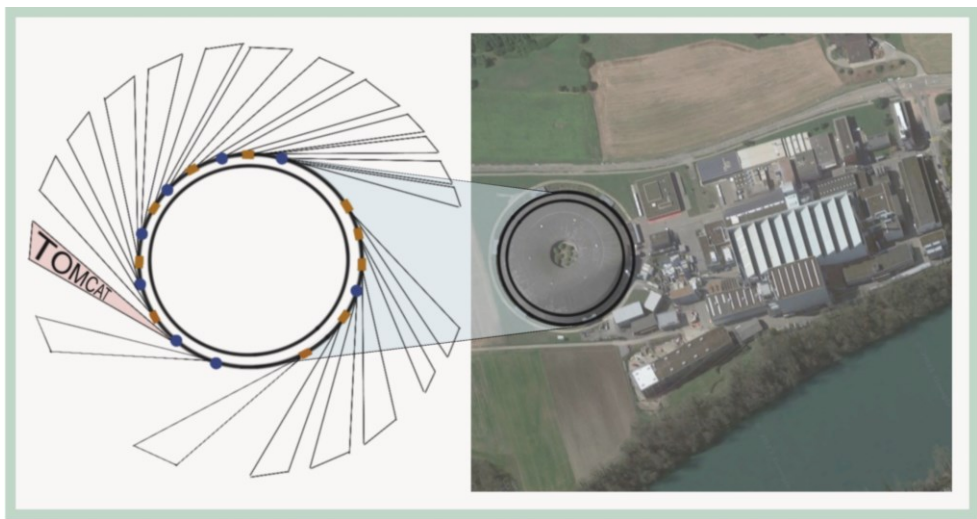
Figure 4 The Swiss light source synchrotron and the beamlines
Figure by My Truong. Adapted from Google maps over the Paul Scherrer Institute.

TOMCAT beamline

As the X-ray pass through the rotating plaque, it is affected by photoelectric interactions and scattering. X-rays that exit the sample towards the detector carry information on these interactions. It is possible to map this information on 2D radiographs that are then reconstructed to 3D tomographic datasets (µCT)(65, 66). Two specific aspects of photoelectric interaction can be mapped(64):

- The material-specific absorption of photons is utilized in absorption contrast tomography (also used in clinical CT).
- The Spatial variations in the refractive index are used in phase-contrast tomography.

The TOmographic Microscopy and Coherent rAdiology experimenTs (TOMCAT) beamline can perform both absorption and phase contrast µCT(66).

Aside from the high resolution and contrast attributed to synchrotron generated X-ray beams, the utilization of different microscopes generates different degrees of magnification(66) (Figure 5)
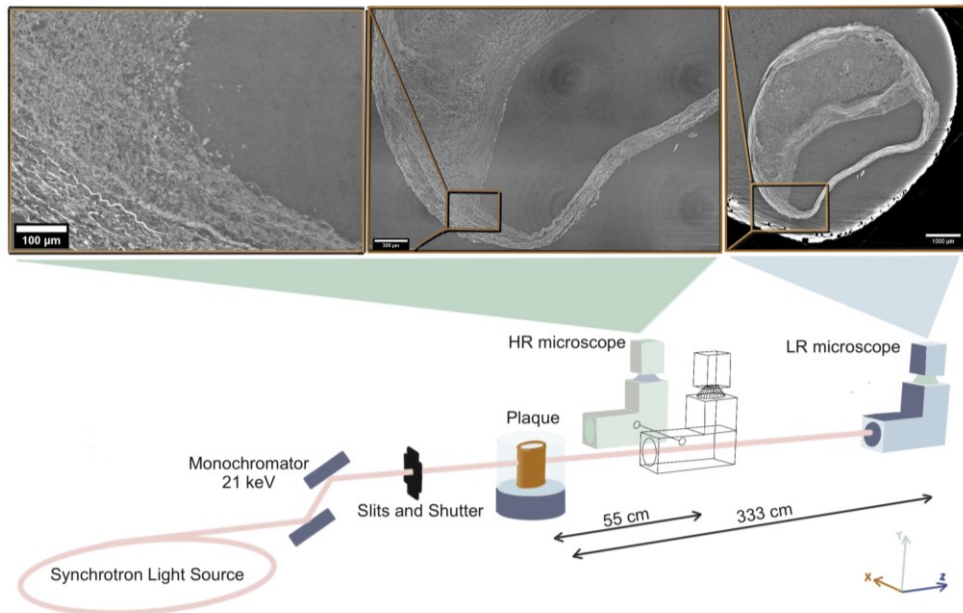
Figure 5 µCT at TOMCAT beamline
Courtesy of Hector Dejea et al. *Comprehensive Analysis of Animal Models of Cardiovascular Disease using Multiscale X-ray Phase Contrast Tomography, Scientific Reports*. Adapted by My Truong.

Phase-contrast μCT

Phase-contrast tomography works on the principle that the photon wave experiences material-specific phase shifts as it propagates through a sample. X-ray waves that propagate through the sample change both amplitude and phase due to refraction and absorption effects. The modulated X-ray wave propagates in free space and develops an interference pattern in a downstream plane behind the sample. These interferences emphasize regions of highly localized changes in the refractive index, such as interfaces between different types of soft tissue. The effect intensifies with increasing distance (the propagation distance) from the sample.

There are many types of phase-contrast X-ray imaging methods. We used propagation-based phase-contrast where we applied a single distance, single material phase-retrieval according to Paganin et al. to acquire the 2D projections that were reconstructed to μCT(67).

Performing phase-contrast CT in a synchrotron takes advantage of the synchrotron X-ray beams' coherence(63). While the attenuation of different tissue is highly similar, the variation in refractive index, together with the beam coherence, permits a better contrast(66). Using the phase retrieval algorithm developed by Paganin(67), signal-to-noise ratio and resolution are maintained at a high level even though dose deposition is the same between absorption and phase-contrast CT.

μCT offers a non-destructive method to study plaques. The entire plaque volume can be scanned without slicing or segmentation. The reconstructed image stack can be analyzed in MPR, where microscopic details on each slice plane are depicted. The method also permits studies of the shape, surfaces, and general architecture of the entire 3D volume.

Computational requirements

μCT and μMRI generate large datasets. Especially synchrotron-based μCT. The size of a Synchrotron-based μ-CT dataset is determined by the pixel size and the bit depth of the detector. We used CMOS cameras with 2048x2048 pixels (LR) and 2560x2160 pixels (HR). With the utilization of a 16-bit depth detector, the stitched reconstructed tomographic datasets generated datasets that ranged between 12.5-260 GB. Post-processing required a workstation with the necessary computational power.

- We used an NVIDIA© graphic card with 2944 GPU cores and 8 GB memory.

- Two separate solid-state hard disks (SSD) for analysis with 500GB each and a mechanical hard drive with 10TB for storage in addition to 4 external hard drives with 4TB storage each. The data was also backed up on a local server at Lund University Medical Radiation Physics department.

- 16 core Central Processing Unit (CPU), with 32 threaded analysis processes.

- System memory (RAM) should be at least two-three times the size of the datasets in a 64-bit operating system. We settled on 128GB for the computer used for the final comparison between µCT and histology. 128 GB was sufficient to work with most of the reconstructed datasets except for some applications on the largest ones (260GB). To process the largest datasets, we used a computer at the Medical Radiation Physics department with 256 GB system memory and the *Ra* computer cluster at PSI. Most of the reconstructions and segmentations were done with the PSI *Ra* computer clusters, both with on-site and off-site access.

Comparing Radiology with Histology

Histology is viewed as the gold standard when evaluating atherosclerotic plaques and validating clinical imaging methods. It can be challenging to compare CT and MRI findings with histology[68] (Fig.6).

Although Histology is a multifaceted and methodologically rich method, it has limitations, is cumbersome, and destructive (to the tissue). The comparison between clinical CTA, ultrasonography (US), digital subtraction angiography (DSA), and MRI with histology can be challenging both in terms of the significant difference in resolution and the fact that histology requires multi-step processing of the excised tissue before the final analysis.

Histologic images can, in my opinion, be viewed as 2D with different thicknesses of sections (typically 5µm thick). The in-plane resolution of histologic images is at best 0.2µm in a conventional light microscope[69]. In contrast, in-plane spatial resolution in the most optimized cardiac CTA could, in theory, be 0.1 mm-0.2 mm (depending on radiation dose). In clinical practice, the in-plane spatial resolution is limited to approximately 0.5 mm using reconstruction algorithms[70]. US has at best axial resolution of 0,1-0,2mm (intravascular US)[71]. MRI spatial resolution depends on camera field strength, scan time, patient movement, and motion correction [57]. The highest resolution of *in vivo* brain scans without motion correction is, to my knowledge, $0.13 \times 0.13 \times 0.8$ mm^3, acquired at 9.4T[58]. The highest resolution in carotid MRI was performed in a 7T unit with voxel size $0.4 \times 0.4 \times 1,5$ mm^3[49]. In paper I, the in-plane resolution was 0.5×0.5 mm^2 interpolated

to $0.3{\times}0.3$ mm^2, with 2mm slice thickness, while in paper III, the acquisition was isotropic with 0.8x0.8x0.8 mm^3 resolution.

We compare images with a thousandfold difference in spatial resolution when comparing in vivo radiologic images with histology.
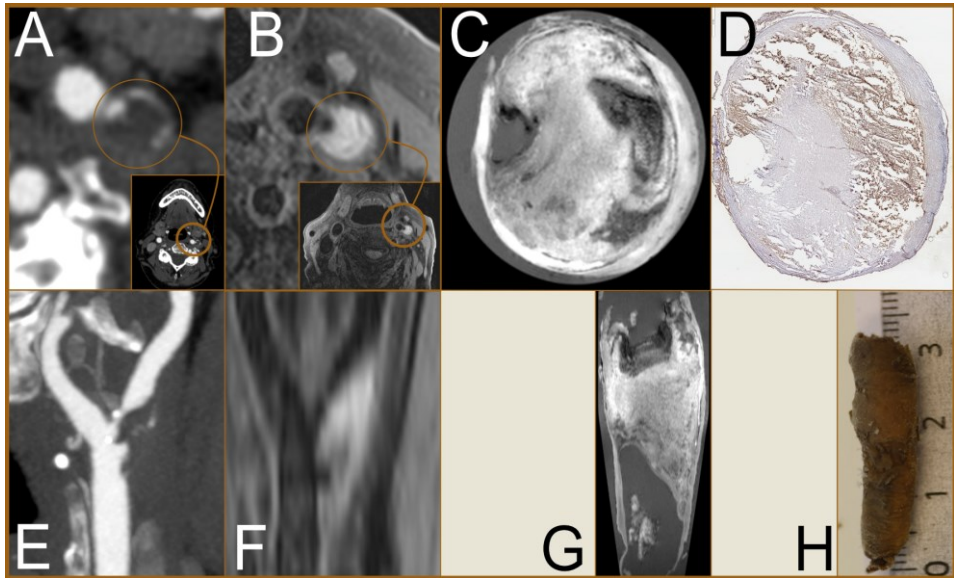
Figure 6. Comparison between radiology *in vivo*, *ex vivo*, and histology.

(**A**) Shows a plaque with IPH on CTA with a high degree of stenosis. (**B**) the corresponding level on *in vivo* MRI with high T1w signal. (**C**) shows the plaque *ex vivo* in 11.7T (T1w). (**D**) is the Glycophorin A stain confirming hemorrhage (brown areas). In (**E**), (**F**), and (**G**), the coronal projection is shown for each modality. (**H**) shows the excised plaque before sectioning.

Aims

The overall aim of this thesis was to use advanced MRI and CT methods to image arterial wall and atherosclerotic plaques with high image and contrast resolution, both *in vivo* and *ex vivo*.

Specific aims of the individual papers were:

I.   To image non-calcified carotid plaque components detected on CTA in stroke or TIA patients, with T1w and 3D T2*w SPGR sequence in 3T *in vivo* MRI to see the relationship between elevated T1w signal and signal loss.

II. To evaluate if ROI data from T1 and T2* maps of symptomatic carotid plaques scanned *ex vivo* in 11.7T MRI, and analyzed with quadratic discriminant analysis (QDA), could with the aid of histology, classify plaque components.

III. To determine whether vessel wall abnormalities in the middle cerebral artery post thrombectomy fit the localization of the lodged thrombus or to the mechanical trauma from the devices used to extract the thrombus. An additional aim was to use prospective motion correction in 7T vesselwall MRI to compensate for patient movement during the examination.

IV. To volumetrically image human carotid atherosclerotic plaques with submicron isotropic voxel size using synchrotron radiation-based µCT to explore the multiplanar and three-dimensionality of typical morphological features in symptomatic plaques-with histological comparison.

Methods

Ethics

The regional ethics committee approved the setup for papers I, II, and IV (Dnr 472/2005, amendment 2014/904, and amendment 2018/63).

The regional ethics committee also approved the setup for paper III (Dnr 2017/794).

Informed and written consent was obtained from all individual participants included in the studies.

All procedures performed in the studies were following the ethical standards of the local ethics committee and with the 1964 Helsinki Declaration and its later amendments.

Software

In paper I, we used SPSS© software to calculate agreement with Cohens Kappa.

In paper II, we used the Statistics toolbox in MATLAB© (version R2019a) to calculate the QDA. The selection of ROI data was made in ImageJ ©, using an in-house written plugin where the high-resolution T1w images were synchronized to the T1 and T2* maps in the axial plane.

In paper II and IV, the histological images were scanned in 20x magnification and viewed in Aperio ImageScope 12.3.2.8013 and 12.4.3.5008©

In paper IV, we used FIJI© and ImageJ© to analyze the image stacks in MPR and reconstruction. Adobe After Effect© software was used for video compilation. Amira software© was used for the segmentation of plaque volumes.

Study populations

Paper I.

Subjects for paper I were recruited at the Neurology ward at the Skåne university hospital in Lund. Patients that had undergone an acute CTA due to TIA or stroke had their exam reviewed for carotid stenosis. In the presence of visible non-calcified plaque components in the carotid bifurcation on the symptomatic side, the patient was asked if they wanted to participate in a study involving MRI of the carotid arterial wall. The MRI was performed while the patients stayed on the Neurology ward for observation, usually within a couple of days.

Paper II.

Plaques in this paper came from the CPIP biobank. The plaques (n12) came from TIA or stroke patients that had been eligible for endarterectomy due to carotid stenosis > 70% on the symptomatic side.

Paper III.

Subjects (N 7) in paper III were recruited from patients that had undergone an acute thrombectomy due to an embolic stroke. Patients who had undergone a successful thrombectomy with recanalization were scanned within two days during their observational stay at the Stroke unit at the Lund Neurology department at Skåne University Hospital. The criteria for inclusion was also that the patient had the physical and cognitive ability to participate in the scan. Some patients that expressed a wish to participate had to be excluded due to worsening of their clinical state before the scan.

Paper IV.

In paper IV, five plaques from the CPIP biobank were included. The plaques were selected based on the criteria that the major portion of the carotid plaque was in one piece and not fragmented.

Study design

Paper I

We used an 8-element phased array surface receive coil (Rapid Biomedical) adapted to a Siemens 3T MRI scanner (Magneton Skyra).

The clinical protocol included pre- and post-Gadolinium-enhanced acquisitions with a total scan time of 22 minutes, shown in Table 1, and sequence information for the two sequences used in the study is shown in Table 2.

The two sequences used to evaluate IPH were a fat-saturated 2D Turbo spin-echo black blood sequence (T1wBB) and a 3D T2*w spoiled gradient echo sequence specific for Siemens, called Multi-echo Data Image combination (MEDIC). Axial slices for T1wBB and 3D MEDIC were positioned perpendicular to the common carotid artery, oriented after a 3D TOF.

Table 1. Carotid clinical protocol
Estimated scan times for each sequence of the MRI protocol. * The post-Gd sequence was not included in this analysis but part of the clinical MRI protocol.

Sequence	Time (min)
Localizer	0:13
TOF 3D	4:08
TSE 2D T1wBB	4:30
3D MEDIC	3:54
Gadolinium (Dotarem®) administration + delay*	5:0
TSE 2D T1wBB+Gd*	4:30

Table 2
MRI sequence parameters for T1wBB and 3D MEDIC.

Sequence parameter	TSE2D T1wBB	3D MEDIC
Acquired in-plane resolution (mm x mm)	0.5x0.5	0.7x0.7
Reconstructed in-plane resolution (mm x mm)	0.3x0.3	0.7x0.7
Slice thickness (mm)	2	0.7
Number of slices	15	60
Repetition time, TR (ms)	750	29
Echo time, TE (ms)	10	16
α°	-	8
Number of echoes	-	3
Turbo spin factor	11	-
Time duration (min: s)	4:30	3:54

Image analysis and statistics

Two experienced neuroradiologists independently reviewed all images. Inter-rater agreement was calculated using Cohen's kappa with a 95% confidence interval. In cases of disagreement between the observers, a consensus decision was reached for the analysis.

The co-localization analysis was done visually, on trans-axial CTA and MRI (3D MEDIC and T1wBB) side by side. The images were synchronized based on distinct morphologic landmarks such as macro-calcifications, plaque shape, and bifurcation.

Areas within the plaque were labeled as *non-calcified plaque components* if the attenuation on CTA images was between 0-200HU and labeled as *calcifications* if the plaque attenuation was 500-1000 HU on CTA. The degree of stenosis on MRI and CTA was calculated by the common carotid artery method (25).

Signal loss on 3D MEDIC was defined as any area within a non-calcified plaque component with signal intensity lower than the ipsilateral sternocleidomastoid muscle. The classification of signal loss was binary and labeled *MEDIC+* if the signal loss was seen and *MEDIC-* if the signal loss was absent.

Elevation of the T1w signal was defined as a higher signal within the plaque component than in the ipsilateral sternocleidomastoid muscle and the common carotid artery on the T1wBB images. The classification was binary and labeled *T1wBB+* if elevated T1w signal was seen and *T1wBB-* if absent.

The result of both reviewers was calculated for interrater agreement with Cohen's kappa with a 95% confidence interval. The percentage of each finding was also documented and compared to each other.

Paper II

The 12 plaques were either snap-frozen in liquid nitrogen or put in Histochoice© upon resection and imaged at the 11,7 T MRI facility at LBIC with high-resolution T1w and T2*w sequences as well as T1 and T2* maps. The image stacks were used to determine optimal cutting levels of the plaque to avoid serial sectioning. We aimed at levels with visible lipid-rich necrotic cores, a high degree of stenosis, and apparent plaque ruptures. Due to the high risk of fragmentation during sectioning, levels with large calcifications were avoided (Fig 7).

The plaques were cryo-sectioned in 8μm transversal slices, and before staining for multiple components, intact sections with visual congruency to MRI were selected. The histologic result was scanned and compared to MRI (Fig. 8).
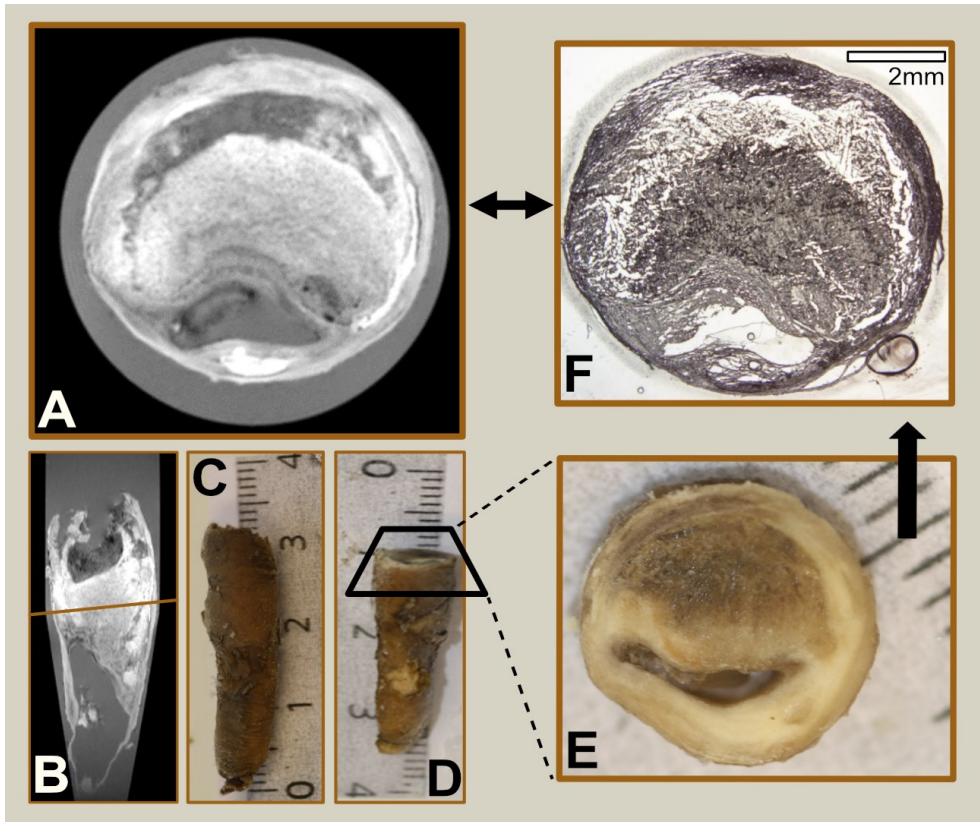
Figure 7 Matching histologic section with the axial plane in multiplanar reconstruction
In **(A),** the plaque is seen in the axial plane in MPR on the T1w high-resolution image. In **(B),** the plaque is seen from a coronal projection with the line indicating the plane seen on (A). The MRI image volume seen in **(A)** and **(B)** is reviewed in MPR to select the appropriate level for sectioning. In **(C),** the intact plaque is seen before sectioning. Guided by the MRI images, the plaque is sectioned proximally to the level of interest **(D)**, with the surface seen in **(E)**. The fragment is further sectioned in the cryo-microtome to the level of interest, and the final section (before staining) is seen in **(F).**
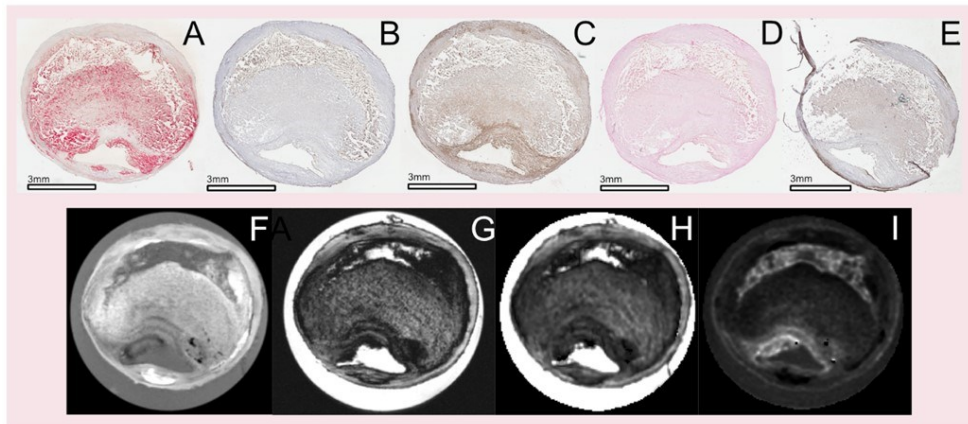
Figure 8 Examples of all five different stains with a matched level in MRI.
The top row shows representative histological images for all five stainings in consecutive sections. **(A)** is Oil Red O staining for lipids. **(B)** is Glycophorin staining for erythrocytes (hemorrhage). **(C)** is CD68 staining for macrophages, corresponding to inflammatory regions. **(D)** is staining for iron in hemorrhage (Perls, negative in this case). **(E)** is Alpha-Actin staining for smooth muscle cells, corresponding in general terms to fibrous tissue. The bottom row shows the corresponding MRI images. **(F)** shows the high-resolution T1w image. **(G)** shows the high-resolution T2w image. **(H**) shows the T2* map, and panel **(I)** shows the T1 map.

Image analysis

The stained sections were used to select ROI on the MRI that contained predefined tissue groups, seen on histology on congruent levels. The process to select ROI was:

i.   The high-resolution T1w images were synchronized to the T1 and T2* maps in the axial plane in ImageJ©, using an in-house written plugin.

ii.   The histological sections of all five types of stainings (erythrocytes, iron, macrophages, calcifications, smooth muscle cells) were matched visually with the corresponding level on the T1w high-resolution images.

iii.   Following morphologic landmarks and guided by the matched histologic section of a specific stain, multiple ROI of 4-9-pixel size were drawn on the HR T1w MRI. Every selected ROI was labeled with the tissue group that the particular stain was representing. Since the HR T1w image was synchronized to the T1/T2* maps, the T1/T2*-values- for all labeled ROI were automatically registered and saved. Fig.9 illustrates an example of the process of selecting and labeling ROI for the lipid group in one plaque and how the T1/T2* values were plotted for the plaque.

Statistics

Mean T1- and T2*-times of each ROI from the maps were plotted on a graph with the mean T1-time on the X-axis and the mean T2*-time on the Y-axis. Every ROI formed one data point on the graph (Fig. 9).

31

We applied quadratic discriminant analysis (QDA) to classify plaque components based on the combination of T1- and T2*-values and other ROI properties such as standard deviations of the T1 and T2* value, maximal and minimal T1 values, and ROI size (number of pixels), all of which were predictor variables for each ROI.

QDA is a statistical method that fits an in-dimensional distribution of each labeled ROI to its predefined class: lipids, inflammation, fibrous tissue, or hemorrhage, by calculating the mean vector and covariance matrix of each tissue group to determine the center and the shape of ROI distribution, respectively. Having fitted the distribution, it is possible to draw boundaries between the tissues by deciding where the ROI's probability is of equal proximity to the center of the group of observations(72). Individual ROIs labeled for a particular tissue group, with parameters that fall under the distribution of another tissue group, are judged as misclassified.
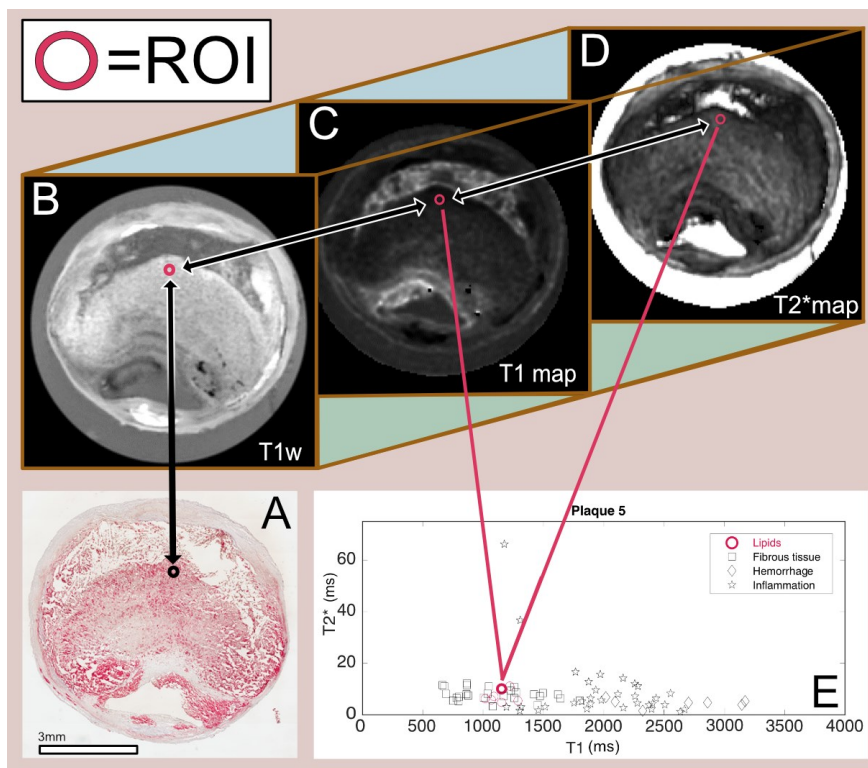
Figure 9. Example of ROI selection validated with histology.
Example of the ROI selection process. In **(A)**, a section stained for lipids is matched visually with the corresponding axial plane in the high-resolution T1w image **(B)**. The high-resolution T1w image stack has previously been synchronized with the T1 map and T2* maps **(C)** and **(D)**, so when an ROI (red circle) is selected on the T1w image, the corresponding ROI on the T1 and T2*maps are automatically selected and sampled. The mean T1/T2* values of each ROI are plotted on a graph **(E)** with the T1 relaxation time on the X-axis and the T2* relaxation time on the Y-axis. Every red circle represents a ROI selected based on the visually matched histological lipid staining in the graph. The process is repeated for all stains and all plaques.

Paper III

7T MRI was performed within two days of a successful thrombectomy in patients with acute stroke. Data collection was between February 2018 and June 2018 at the Swedish National 7T facility at Lund University Bioimaging Center. Sequence details in the protocol are listed in Table 3. The sequence used was a 3D Magnetization Prepared Inversion Recovery-Turbo Spin Echo (MPIR-TSE), a volumetric black blood sequence with an inversion pulse to null CSF, and magnetization preparation to increase SNR, described in detail by van der Kolk et al.(51, 52). This sequence was performed before gadolinium contrast administration and three minutes after.

Table 3
7T MRI sequence parameters

Parameters	3D TFE[3]	3D MPIR-TSE[4]	iMOCO 3D Fat Navigator	2D flow
Acq. Res. (mm×mm)[1]	1×1	0.8×0.8	7×7	0.5×0.5
Recon. Res. (mm×mm)[2]	1×1	0.5×0.5	5.2×5.2	0.5×0.5
Slice thickness	1	0.8	7	3
Number of slices	190	238	21	1
Repetition time, TR (ms)	5	3952	3	15
Echo time, TE (ms)	2	38	1.38	4.8
α°	6	68	4 (binomial, fat-selective)	7
Echo train length[5]	450	156	-	2
Inversion time, TI (ms)	-	1375	-	-
Velocity sensitivity, Venc (cm/s)	-	-	-	200
SENSE factor	2×2	2×3	2×2	2
Partial Fourier factor	-	-	0.85×0.85	-
Dynamic scan time (ms)	-	-	484	-
Time duration (min: s)	1:37	10:32*	-	1:35

[1]Acquired inplane resolution, [2]Reconstructed inplane resolution. [3]Turbo Field Echo, [4]Magnetization Prepared Inversion Recovery-Turbo Spin Echo, [5]For TFE: Turbo Field Echo factor, for TSE: echo train length * Including the 3D fat navigator

Motion correction

To reduce motion artifacts that cause blurring of the vessel walls, an interleaved prospective motion correction using a newly developed navigator framework (iMOCO)(73) was applied to the 3D MPIR-TSE sequence. For quantifying motion, fat-selective 3D gradient-echo navigator volumes (74) were inserted in the time gaps after each TSE readout in the 3D MPIR-TSE sequence. Each reconstructed navigator volume was compared to the first volume in real-time. The position and angulation of the MPIR-TSE volume were correspondingly updated before the next repetition of the MPIR-TSE. Furthermore, a motion score combining translation and rotation was calculated (75). If the detected motion exceeded a certain threshold (1

mm in this protocol), the last shot of the MPIR-TSE was reacquired using the updated geometry settings. Reacquisition prolongs the scan duration but reduces motion artifacts. This way, the patient's motion was detected and monitored on the operator console during acquisition, allowing the operator to see the amount of movement and reacquisitions during the scan (Fig. 10).
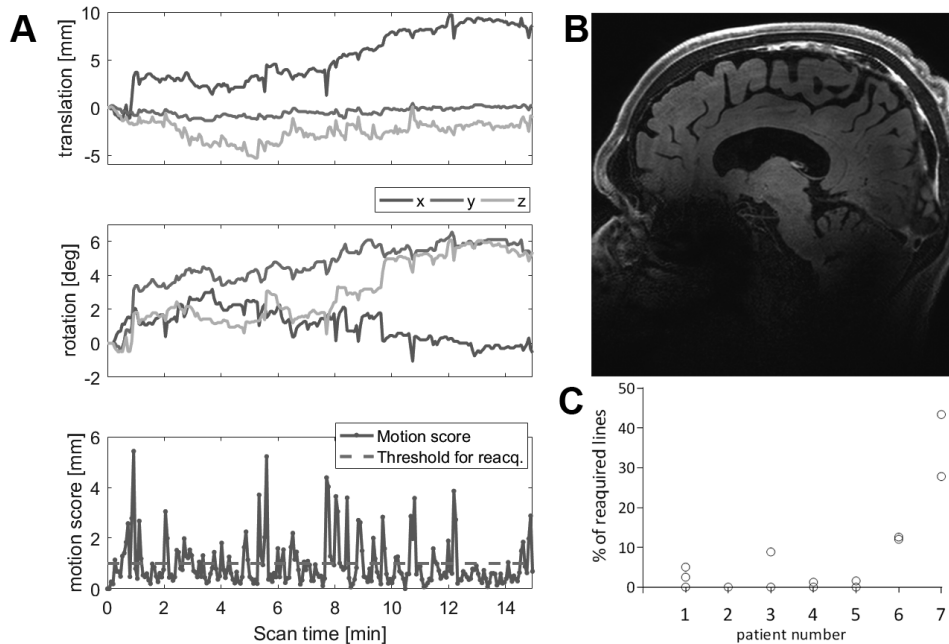
Figure 10 Effects of prospective motion correction.
The monitored motion during the post-Gd acquisition for the patient that moved the most **(A).** The translations (top left panel) show the translation in millimeters in x, y, and z rotations (middle left panel) shows the position relative to the start in degrees. During the scan, the motion score (bottom left panel) is continuously monitored. In this case, the patient moved almost 1 cm and rotated up to 6°. Motion larger than the chosen threshold (dashed line in the lower-left panel, set to 1 mm in our protocol) triggers reacquisition of the previously acquired k-space segment. Despite this severe motion, the image quality was excellent, as shown by an image from the same acquisition **(B).** The percentage of reacquired data for all 14 vessel wall scans clearly showing that the movements in patient 6 and 7 demanded reacquisition of a large part of the data **(C).** Courtesy of Mads Andersen

Image Analysis

Image analysis was performed independently by two neuroradiologists. The final analysis was undertaken at least three months after the MRI examination to minimize the risk of recall bias.

The vessel wall was assessed, and gadolinium contrast uptake was noted. According to pre-Gd and post-Gd images, the level of motion artifacts was graded according to a pre-defined scale. The overall image quality of the pre-Gd and post-Gd images was graded according to another pre-defined scale.

The location of any Gd-uptake was correlated to the location of the embolus based on the pre-operative CTA and the location of the stent-retriever based on the pre-operative DSA (Fig.15).

We analyzed flow data with Segment v2.2R6324 (http://segment.heiberg.se) (76). After performing a linear background correction, quantitative values on flow, flow rates, and velocities were obtained.

Paper IV

Sample preparation and study workflow

We originally planned to compare *ex vivo* 9.4T µMRI and synchrotron-based phase-contrast µCT with histology in paper IV. The plaques were initially fixated in 4% formaldehyde, stored in 70% ethanol but transferred to distilled water for the MRI scan, moved back to ethanol, and then embedded in paraffin. We did not expect that this would affect plaque morphology since the transfer from different mediums was iterative. Due to an extensive amount of collected data, we decided to start with a comparison between µCT and histology.

We scanned the plaques embedded in paraffin with synchrotron-based propagation phase-contrast µCT. The plaques were scanned with multiple navigational low-resolution synchrotron radiation-based micro-computed tomographies (LR SRµCT) with 6.5 µm voxel size for overview. The field of view (FoV) for each scan was $13.3x13.3$ mm^2 (2048x2048 pixels) in the axial plane, which covered each plaque's entire axial surface. By stitching multiple consecutive LR SRµCT reconstructed volumes orthogonal to the beam direction, we also covered the full plaque length, which gave us an overview of each plaque. The data sets were stitched and reconstructed according to the method described by Miettinen and Paganin et al. (65, 77).

Guided by the LR SRµCT, we scanned areas that showed specific atherosclerotic pathological characteristics with multiple high-resolution synchrotron radiation-based computed tomographies (HR SRµCT) with 0.65 µm isotropic voxel size. The FoV for each HR SRµCT scan covered $1404x1664x1664$ µm^3. Multiple adjacent and partially overlapping scans were reconstructed individually and stitched together to maximize the axial plane coverage (figure 17). The iterative increase in resolution was chosen to facilitate overview, orientation, and comparison to histology since most HR SRµCT did not cover the entire axial plaque surface.

Figure 17 shows an example of the 3D volume of a plaque and the workflow of how the overview scan guided us in analyzing the HR µCT and in the comparison to histology.

After μCT, guided by the navigational low-resolution scan, the plaques were microtomed to 6μm sections at levels that matched the high-resolution μCT. The resulting sections were stained for macrophages, erythrocytes, smooth muscle cells, calcifications, iron, collagen, reticular fibers, elastic fibers, ground substance, fibrin, and mucin. The multiple histologic stains were compared to the reconstructed μCT.

Synchrotron radiation μCT at TOMCAT beamline

We used a multilayer monochromator with the x-ray beam energy set to 21 keV. The scans were done in parallel beam geometry, and the sample was rotating over 180 degrees during the tomographic acquisition (Fig.11)
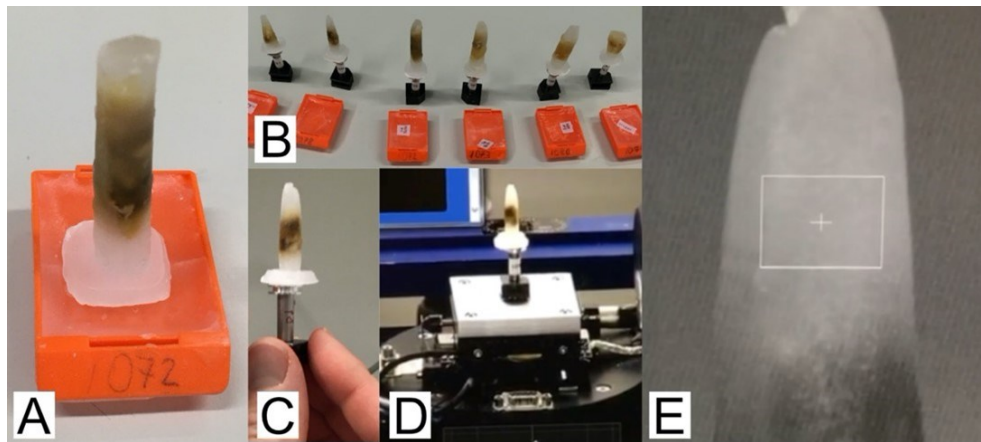
Figure 11. Plaques
An example of a paraffin-embedded plaque is shown in (**A**.) In (**B**), all five plaques mounted on pins are displayed (the 6th plaque to the right was never scanned). In (**C**), a mounted plaque is seen up-close, and in (**D**), the plaque is placed in the tomography setup at the beamline. (**E**) shows an image of the plaque taken from an optical camera used for pre-aligning the sample before the tomographic scan.

For technical details, please be referred to paper IV in the appendix in the printed version of the thesis.

For each plaque, multiple LR SRμCT scans were needed to cover the entire sample. They were afterward stitched together orthogonally to the beam direction to cover the full plaque length.

Following the LR acquisitions and reconstructions of each sample, selected regions of interest (ROIs) were identified. Those ROIs were then scanned with multiple HR SRμCT. The energy was still set to 21 keV for these scans, but we used a 10x microscope. The result had an effective pixel size of 0,65 μm. To optimize the area of transaxial coverage, multiple adjacent and overlapping HR SRμCT acquisitions were made. As for the LR, they were reconstructed and stitched together afterward, as described by Miettinen et al. (65). Scan parameters are listed in table 4.

Table 4. SR µCT parameters

Parameters	Low-resolution scan	High-resolution scan
Camera	pco.edge 4.2 sCMOS	pco.edge 5.5 sCMOS
Resolution	2048x2048	2560x2160
Pixel size (µm)	6.5	6.5
X-ray camera optics	1x	10x optics
Effective pixel size (µm)	6.5	0.65
Scintillator	300 µm LuAg:Ce	20 µm LuAg:Ce
Beam Energy (keV)	21	21
Beam geometry	Parallel	Parallel
FoV at sample position	570 pixels*6.5 µm =3,705 mm vertically 2048 pixels*6.5 µm = 3,260 mm horizontally	2560pixels*0.65 µm =1,664 mm vertically 2160pixels*0.65 µm =1,404 mm horizontally
Sample rotation (degrees)	180	180
Absorbers, Filters	5 mm pyrolitic graphite, 400 µm Al, 10 µm Fe	100 µm Al, 10 µm Fe
Projections	1501	1501
Exposure time (ms)	30	200
Sample-Detector distance (mm)	3300	55
Flat-field images	100	100
Dark-field images	30	30
Scan time per CT (min:s)	2:04	6:33

Histologic method

After SRµCT, the paraffin-embedded plaques were prepared to remove the paraffin. They were macroscopically cut with a Jewelers' saw. Tissue loss of the saw was 0.254 mm at the cutting plane. The plaques were divided into 2-5 mm-thick fragments, re-embedded in paraffin, and sectioned to 6 µm in the microtome.

The LR SRµCT guided us to select section planes, and we aimed at acquiring sections visually congruent with HR SRµCT axial planes. Sections were viewed in a light microscope alongside microtoming and continuously compared to the µCT images. When the histologic section's overall morphology showed visual congruency with the corresponding level plane on LR SRµCT and HR SRµCT, 6µm thick sections were saved for different stainings. We stained for macrophages, vascular smooth muscle, erythrocytes, calcifications, collagen, reticular fibers, elastic fibers, ground substance, fibrin, and mucin. Technical details of the immunohistochemical and histological process are described in paper IV in the appendix. All stained sections were scanned to digital images in 20x magnification.

Image processing and analysis

All stitched LR SRµCT and HR SRµCT scans for each plaque were analyzed as 16-bit TIFF sequences and viewed as image stacks. Areas with typical plaque pathology were selected, compared to histology, and sub-volumes and segmentations were performed and selected for movie compilation and volume rendering. Volumes used for visualization were downscaled for a smoother workflow.

Results

Paper I

Patient data

Between September 2014 and July 2016, 1280 consecutive CTA were screened for candidates, and the 46 patients that met all inclusion criteria were considered for inclusion. Four of these had contraindications to MRI that was not known at inclusion or withdrew from participation after the initial consent.

Of the 42 patients that completed the MRI examination, 3D MEDIC images were non-diagnostic, typically due to patient motion, in 8 patients, resulting in 34 patients with a complete set of diagnostic images for the final image analysis (Table 5)

The median degree of stenosis, calculated by the common carotid artery method, was 70% on CTA (Interquartile range (IQR)= 50-88%) and MRI (IQR= 60-88%).

Table 5 Demographic data
All patients with a complete set of diagnostic images.

Variables	(n)
All patients with complete imaging (n)	34
Median Age (total range, IQR)	72,5 (35-86, 66-78)
Female (%)	11 (32)
Indication	
TIA n (%)	11 (32)
Stroke n (%)	23 (68)
Degree of stenosis %	
CTA median (total range, IQR)	70 (35-95, 50-88)
MRI median (total range, IQR)	70 (35-95, 60-88)

Image analysis and statistics

All areas with macro-calcifications on CTA showed corresponding signal loss on 3D MEDIC. Most plaques (26/34, 76%) had a signal loss within the non-calcified component on 3D MEDIC. Less than half of the plaques 14/34 (41%) had an elevated T1wBB signal within the non-calcified component, suggestive of the presence of methemoglobin.

An elevated signal on T1wBB and signal loss on MEDIC was seen within a non-calcified component in 13/34 (38%) of the patients. An elevated signal on T1wBB without signal loss on MEDIC within a non-calcified plaque component was seen in 1/34 plaques (3%). Signal loss on MEDIC without elevated signal on T1wBB was seen within a non-calcified plaque component in 13/34 (38%).7/34 (21%) had neither elevated signal on T1wBB nor signal loss on MEDIC.

Cohen's kappa for inter-reader agreement was 0.64 (CI 0.345-0.925) for 3D MEDIC and 0.94 (CI 0.81-1.00) for T1wBB.

The image analysis results are shown in Table 6, and the corresponding typical patterns are illustrated in Figure 12.

Table 6. The distribution of signal loss on 3D MEDIC and elevated T1w signal on the T1wBB.

Cross table with the distribution of the presence or absence of signal loss on 3D MEDIC and T1w signal elevation in the 34 plaques. The four groups have the same color representation as used in Figure 12.

	Signal loss 3D MEDIC +	No signal loss 3D MEDIC -	
T1w +	13/34 (38%)	1/34 (3%)	14/34 (41%)
T1w -	13/34 (38%)	7/34 (21%)	20/34 (59%)
	26/34 (76%)	8/34 (24%)	
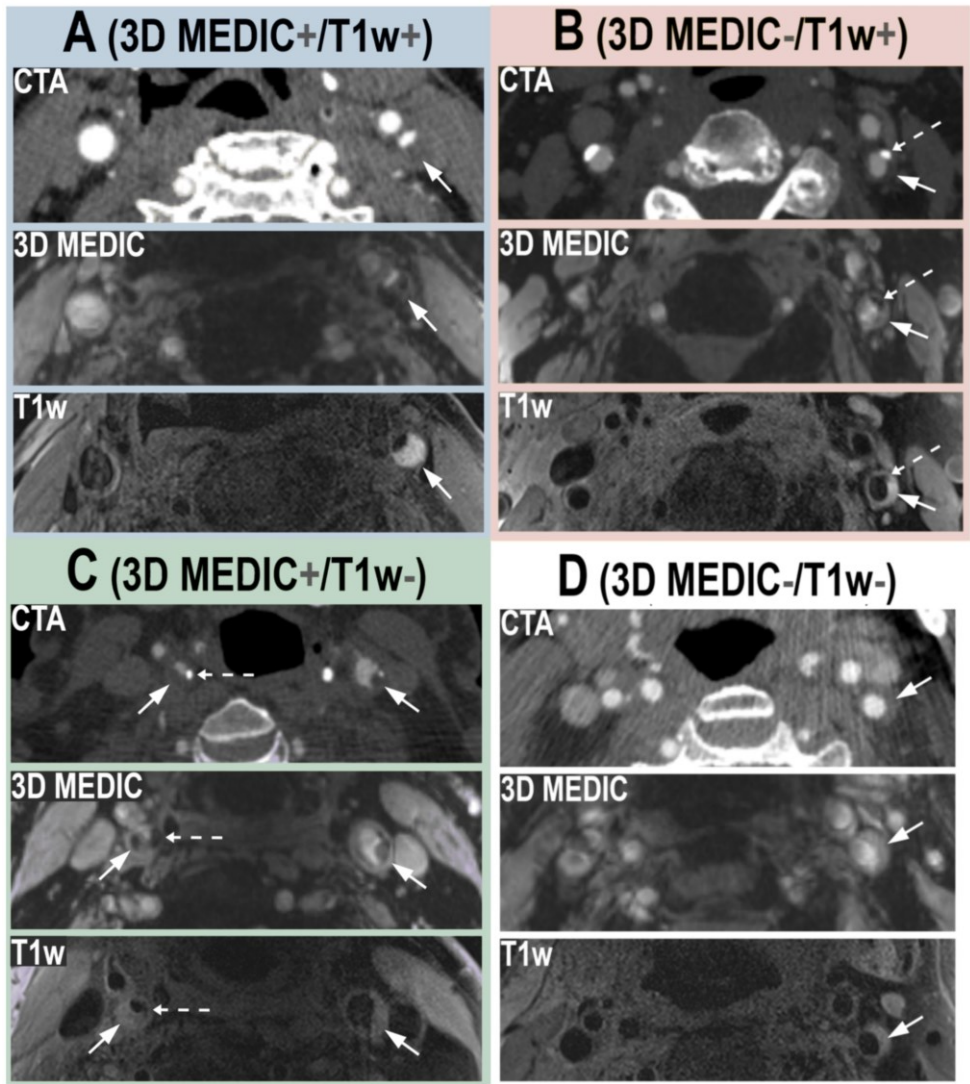
Figure 12. Typical imaging findings for each of the four groups at the level of the carotid bifurcation on CTA, 3D MEDIC, and T1wBB, described in table 6, with the same color representation.

In **panel A**, in blue color, the arrow indicates a large non-calcified plaque component with a signal loss on 3D MEDIC and elevated T1w signal (**3DMEDIC+/T1w+**). In **panel B**, in pink color, the arrow indicates a non-calcified plaque component with no signal loss on 3D MEDIC and elevated T1w signal (**3DMEDIC-/T1w+**). The dotted arrow indicates a calcification, with high attenuation on CTA, signal loss on 3D MEDIC, and signal loss on T1w. In **panel C**, in green color, the filled arrows on both sides indicate large non-calcified plaque components with a signal loss on 3D MEDIC and no elevation of Tw1 signal (**MEDIC+/T1w**). The dotted arrow on the left side shows a calcification, with high attenuation on CTA, signal loss on 3D MEDIC, and signal loss on T1w on the asymptomatic side (this side was not included in the final image analysis). In **panel D**, in white color, the arrow indicates a small non-calcified plaque without signal loss on 3D MEDIC and no T1w signal elevation (**MEDIC-/T1w-**).

Paper II

Patient data

During the inclusion period, 46 potential candidates were identified based on clinical data and acute CTA. Of these 46 patients, 15 were accepted for surgery and offered to participate in the study. Two patients chose not to participate. One additional patient admitted for surgery was not operated on due to deterioration in clinical status. The remaining 12 plaques from 12 patients were imaged and included in the final analysis. The plaques were included in the CPIP biobank. Patient and plaque data is shown in Table 7.

Table 7. Patient data

Number of patients	12
Median age [range]	75 years [63-86]
Sex (M/F)	10/2
Event (TIA/stroke)	6/6
Days from event to surgery (median [range])	12 [5-31]
Days from surgery to MRI (median [range])	52 [9-420]
Fixation at surgery (Histochoice©/Snap frozen)	9/3

Images and classification

Visual agreement of in-plane matching between histology and MRI was accomplished in all plaques, in a total of 70 sections. All 12 plaques contained lipids, areas with inflammation, fibrous tissue, and hemorrhage, but only the stained sections matched with MRI were included in the ROI-selection process.

A total of 965 ROIs were analyzed: 407 fibrous tissue, 250 lipids, 184 of inflammation, and 124 as hemorrhage.

- Fibrous tissue was matched between histology and MRI in all plaques.
- Lipids were matched in 10/12 plaques.
- Tissue with inflammation was matched in 9/12 plaques.
- Hemorrhage was matched in 5/12 plaques.

ROI distribution of plaque components and misclassification rate from the QDA is shown in Figure 13.
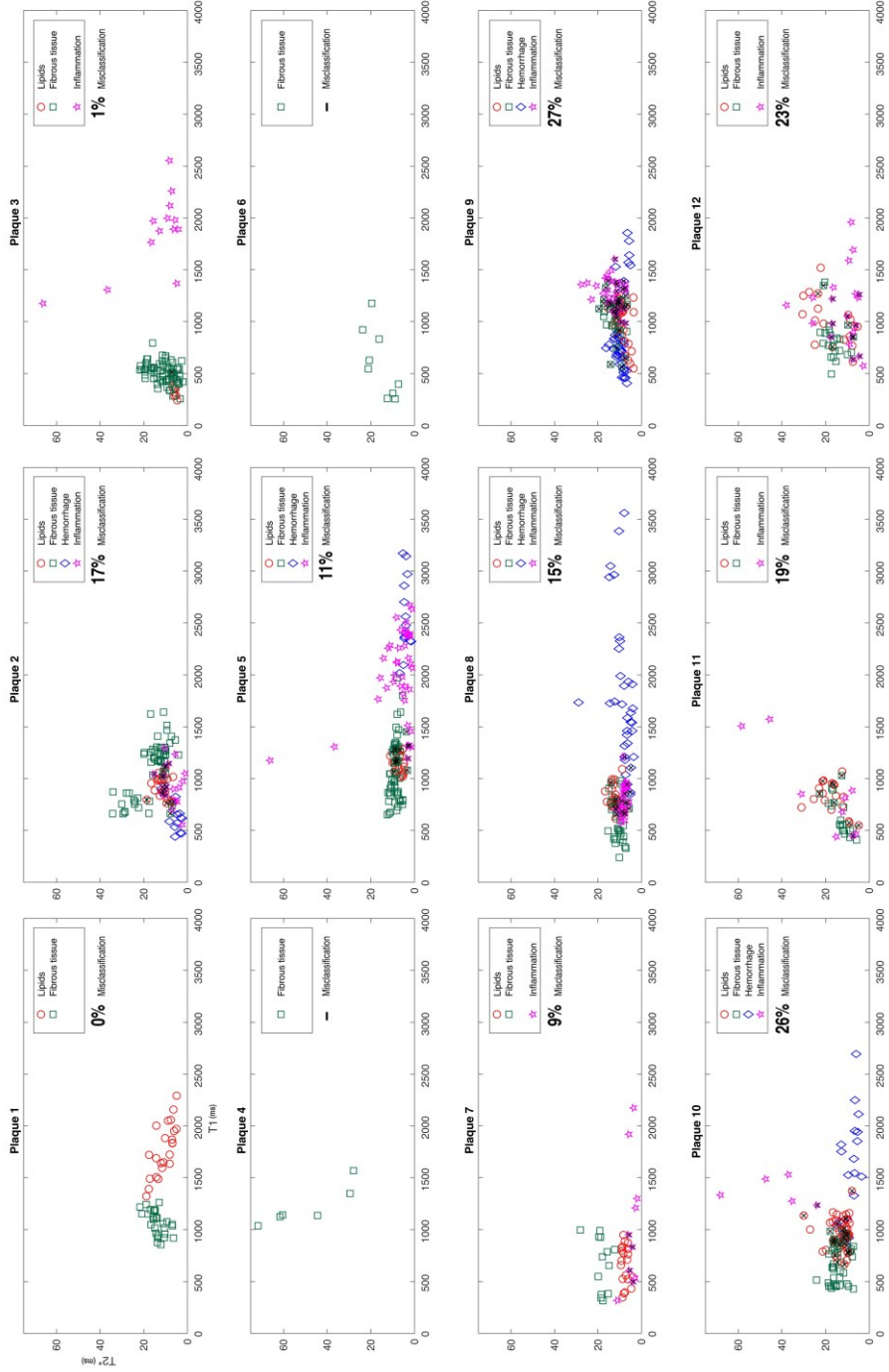
Figure 13. ROI distribution and misclassification rate of all 12 plaques

The plaque with zero misclassification contained predominantly fibrous tissue and lipids and no ROI for hemorrhage or inflammation that could be matched with histology (Figure 13). Nine out of 12 plaques had either inflammation or hemorrhage or a combination, as well as lipids and fibrous tissue that could be matched between histology and MRI. The mean percentage of misclassified ROI was 16,5% (CI 11.0-22.0). Two of the plaques contained predominantly fibrous tissue, and QDA was therefore not applicable. In Figure 13, the misclassification rate calculated with QDA for each plaque is shown in percentage, and the misclassified ROI is indicated with an overlapping X.

The largest range of T1 values (~400-3560 ms) was seen in hemorrhage, and the smallest range (~440-1970 ms) in fibrous tissue (Table 8). The largest range of T2* values (~2-70 ms) was seen in fibrous tissue, and the smallest range of T2* values (~2-29 ms) in hemorrhage. The range may be even smaller since the hemorrhage ROI with the highest value (~29) might be an outlier. Without the outlier, the range of T2* values for hemorrhage was ~2-16 ms (Table 8). Figure 14 shows the distribution of ROI for each tissue class.

Table 8. ROI data

Parameter	ROI (n)	Min (ms)	Max (ms)	Mean (ms)	Std dev. (ms)	Range (ms)
Lipids mean T1	250	241.03	2290.56	994.98	338.93	2353.67
Inflammation mean T1	184	317.14	2670.81	1317.74	555.95	2049.53
Hemorrhage mean T1	124	406.08	3560.94	1393.45	774.46	3154.87
Fibrous tissue mean T1	407	239.36	1970.11	836.18	322.36	1730.75
Lipids mean T2*	250	3.59	31.00	11.38	5.17	27.42
Inflammation mean T2*	184	1.14	68.15	11.35	11.26	67.01
Hemorrhage mean T2*	124	1.55	28.98 (16)	8.10	3.77	27.43 (14.67)
Fibrous tissue mean T2*	407	2.04	71.64	13.23	7.14	69.60
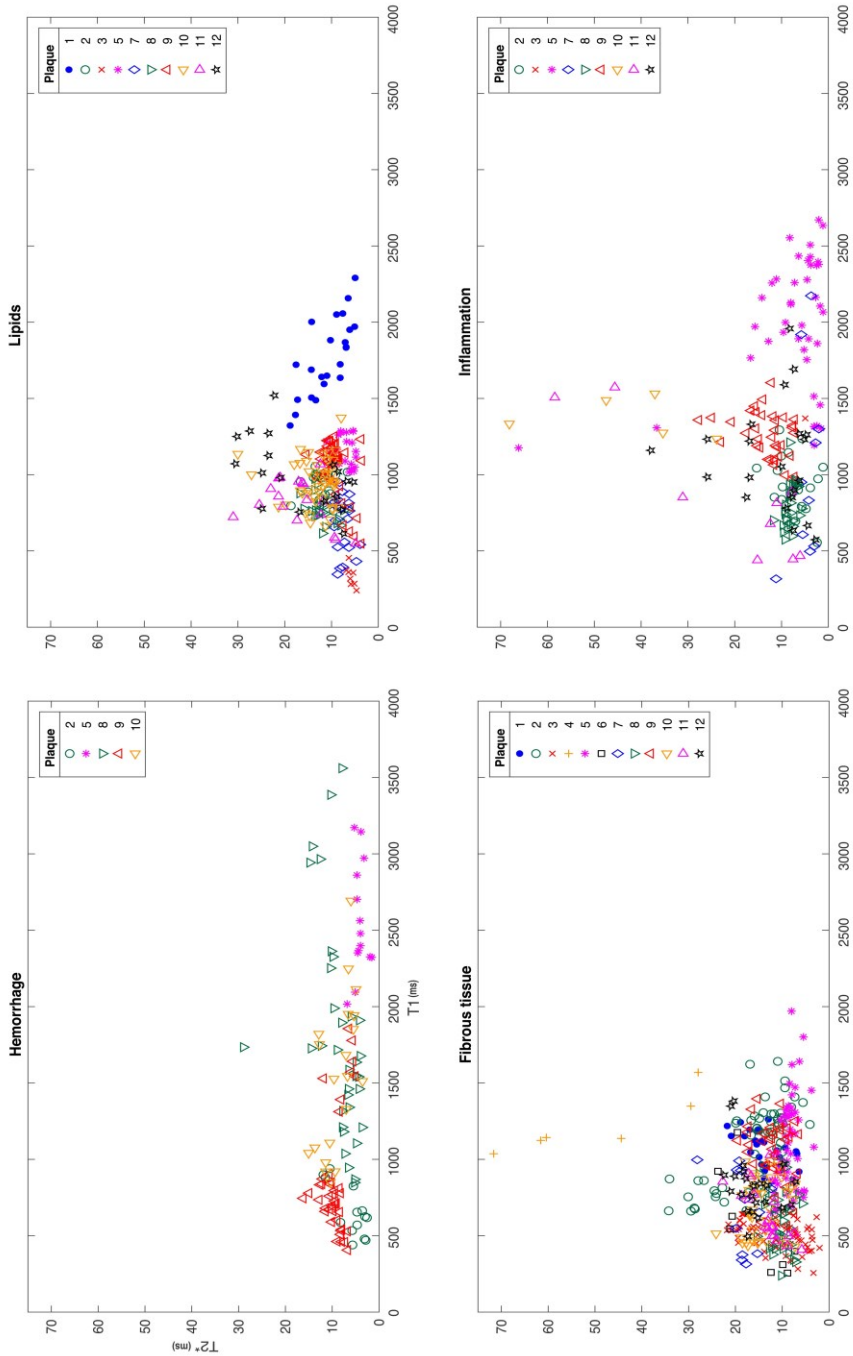
Figure 14. Distribution of ROI data for each tissue class.
The distribution of the combination of T1/T2* relaxation times for ROI of lipids, fibrous tissue, inflammation, and hemorrhage, for each plaque.

Paper III

Patient data

Patients (n = 7, mean age 69 years, range 55–84 years) treated with endovascular thrombectomy for acute stroke in the anterior circulation with a CTA-verified thrombus in the distal internal carotid artery (T-occlusion), or M1- or M2-segments of the middle cerebral artery from February 2018 to June 2018 were included in the study. Patient data is listed in Table 9. All examinations were performed without sedation. In figure15, one example of the image analysis of all modalities is shown. In general, all patients tolerated the study well. For one patient, there was significant motion during the post-contrast MPIR-TSE, but the scan was aborted early and then reacquired.

Table 9. Patient data
Patient data including Age, Sex, affected side, NIHSS (National Institute of Health Stroke Score) before treatment, treated vessel segment (M=Middle Cerebral Artery, T= Distal Carotid "T-occlusion"), TICI-score, the name of the stent retriever used, and the number of days between treatment and MRI examination.

Patient	Age	Sex (M/F)	Affected side	NIHSS Pre-treatment	Treated vessel	Number of attempts	TICI score	Stent retriever	Days between treatment and MRI
1	80	F	R	1	M1	1	2B	Solitaire 4/40	2
3	61	F	L	5	M2	1	2B	Embotrap 5/33	2
4	84	F	R	3	M2	1	3	Embotrap 5/33	1
2	69	F	R	9	M1	2	2B	Embotrap 5/33	2
5	74	F	L	20	M2	1	3	TREVO 4/40	2
6	55	M	R	8	M1	1	3	Solitaire 4/40	1
7	67	M	R	20	T+M1	1	3	Solitaire 4/40	1
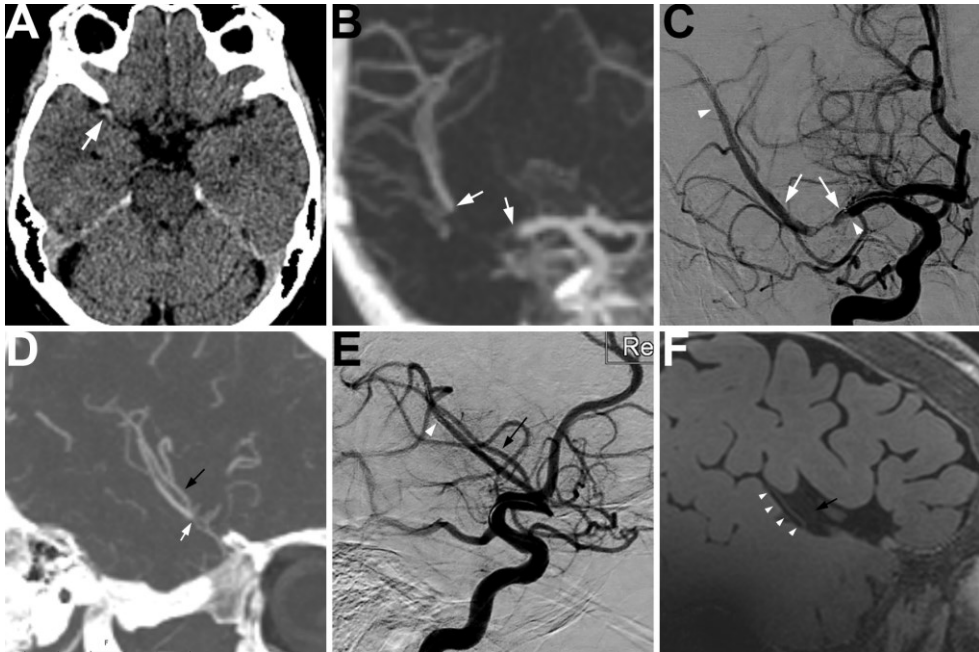
Figure 15. Illustration of typical findings in one of the patients.
(a) The site of the embolus was determined from the dens artery sign on non-enhanced CT (white
arrow), (b) occlusion on CTA (white arrows indicating the proximal and distal end of the embolus), and (c) DSA
images from the thrombectomy procedure (white arrows indicating the proximal and distal end of the embolus, white
arrowhead indicating the distal end of the stent retriever). The dominant M2 branch distal of the embolus in which the
stent retriever was deployed (the white arrow in panel D indicates the distal end of the embolus, the white arrowhead
in panel E indicating the distal end of the stent retriever) shows vessel wall Gd uptake corresponding to the entire
length of the stent retriever (white arrowheads in panel F. (d–f) The black arrows illustrate another M2 branch distal of
the occlusion that shows no vessel wall Gd uptake

Image analysis

Both reviewers identified vessel wall Gd uptake on the side that had been treated
during the thrombectomy. In all cases, both reviewers agreed that the Gd uptake
correlated to the location of the stent retriever rather than to the site of the embolus
(Table 10 and 11, Figure 16)). The agreement between reviewers was excellent. The
results of the image assessment by the two neuroradiologists are shown in Table 10.

Overall image quality was graded highest on a 3-grade scale (1=non-diagnostic,
2=acceptable, 3=excellent) for all patients in all contrast phases by both reviewers.
Motion artifacts were rated as *none* or *not affecting diagnostic quality* for all
examinations by both reviewers. Neither reviewer rated the motion artifacts as
impairing the diagnostic quality for any case.

Table 10. The results of the MRI imaging assessment
by the two blinded reviewers (Reviewer 1/Reviewer 2) for the side of vessel wall gadolinium contrast (Gd) uptake, correlation with the location of the embolus, the stent retriever or both, overall image quality on the pre- and post-contrast acquisitions (*), the degree of motion artifacts (†) in the post-contrast acquisitions, and presence of Large Vessel Occlusions.

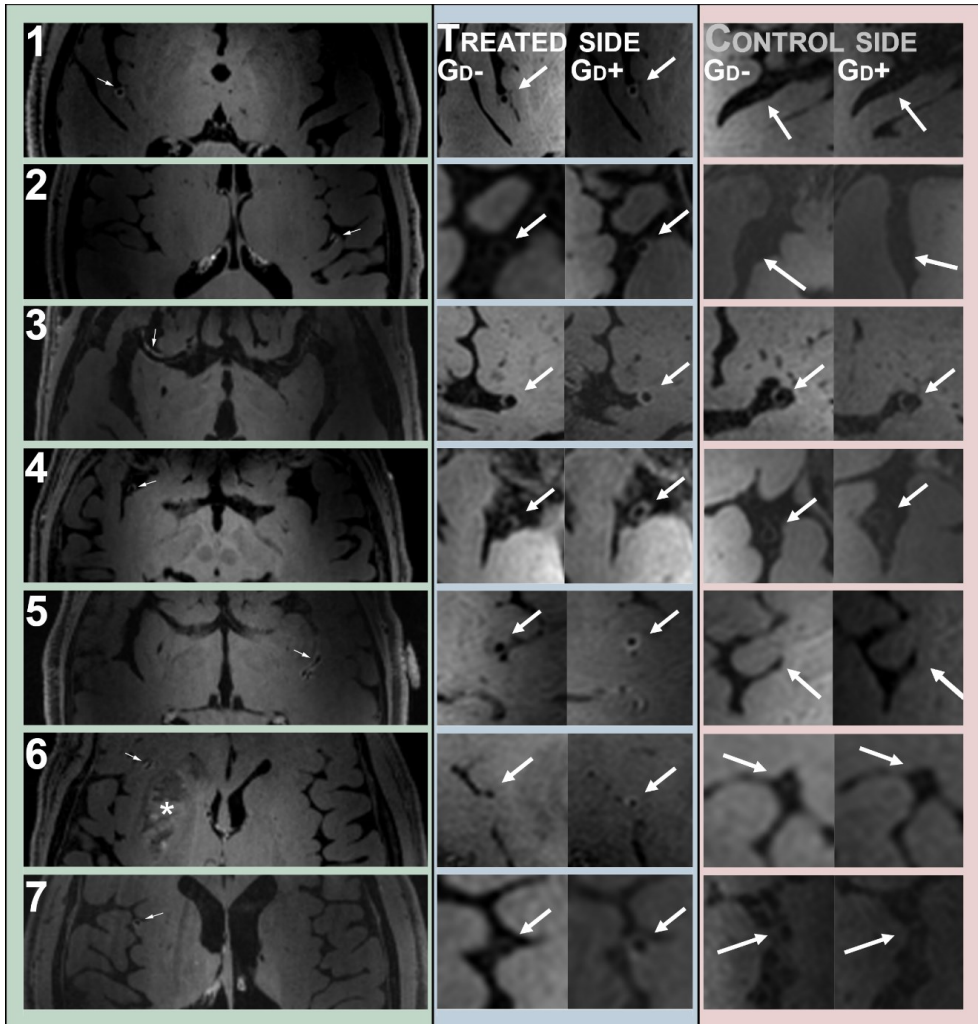†: Level of Motion Artifacts: 1=None, 2=Visible but not affecting Image Quality, 3=Impairing Image Quality

*: Overall Image Quality: 1=Non-Diagnostic, 2= Acceptable, 3=Excellent

Patient	Gd Uptake Side (R/L)	Gd Uptake Correlation (Embolus, Stent-retriever or Both)	Image Quality Pre Gd (1-3) *	Image Quality Post Gd (1-3) *	Motion Artifacts (1-3) †	Large Vessel Occlusion (Yes/No)
1	R/R	Stent/Stent	3/3	3/3	1/1	No/No
3	L/L	Stent/Stent	3/3	3/3	2/2	No/No
4	R/R	Stent/Stent	3/3	3/3	2/1	No/No
2	R/R	Stent/Stent	3/3	3/3	2/1	No/No
5	L/L	Stent/Stent	3/3	3/3	2/1	No/No
6	R/R	Stent/Stent	3/3	3/3	2/2	No/No
7	R/R	Stent/Stent	3/3	3/3	2/2	No/No

Table 11. Image analysis data of the MRIR-TSE
Hyperintensity previous to gadolinium contrast administration on the affected side (ipsilateral) and the contralateral side, wall thickness with/without contrast, any visible vessel wall edema on the ipsilateral side/contralateral side, and the length of vessel wall enhancement.

Patient	Hyper-intensity Pre-Gd ipsilateral	Hyper-intensity Pre-Gd Contra-lateral	Wall thickness pre-Gd ipsilateral (mm)	Wall thickness post-Gd ipsilateral (mm)	Wall edema ipsilateral side	Wall edema contra-lateral side	Length of wall enhancement (mm)
1	No	No	0.7–1.30	1.3–1.6	Yes	No	53
3	No	No	0.7–0.8	1.0–1.2	Yes	No	86
4	No	No	0.7–1.0	0.9–1.3	Yes	No	51
2	No	No	0.5–0.9	0.8–1.2	Yes	No	62
5	No	No	0.7	1.1–1.4	No	No	45
6	No	No	1.0	1.0–1.4	No	No	32
7	No	No	0.8	1.3–1.4	No	No	53

Figure 16. Transaxial images post-Gd images from all seven subjects

Gd uptake in the vessel walls corresponds to the position of the stent retriever (arrows in **green** (left) and **blue** (middle) column, with the absence of Gd uptake on the contralateral side (**pink** right column). The asterisk indicates a basal ganglia infarct in patient 6. All images in the **green** left column were reconstructed from sagittal acquisitions to transaxial reconstructions. The images in the **blue** (middle) and **pink** (right) columns were reconstructed to obtain image planes perpendicular to the center-line to illustrate the circumferential distribution of vessel wall edema pre-Gd (**blue** middle column Gd−) and the post-Gd enhancement (**blue** middle column Gd+). On the contralateral side (**pink** right column), the vessel vas often barely visible, and in cases where the vessel was occasionally thicker, suggesting intracranial atherosclerosis, little or no Gd-uptake was seen (illustrated in patient 3/control Gd− and Gd+)

Motion correction

In total, 14 MPIR-TSE sequences were acquired. In eight of these, the motion never exceeded the reacquisition threshold, so the scan time was unaffected. In the remaining six MPIR-TSE scans, the percentage of reacquired data was between

1.6% and 43% (median 11%), which corresponds to a scan prolongation of between 10 s and 3:39 min, respectively (median 61 s).

Figure 11(a) shows the motion observed for the patient that moved the most. The patient moved gradually, almost 1 cm in the x-direction, and rotated 5-6 degrees around the y and z-axis during the scan. Motion larger than the threshold (dashed line in the lower panel in Figure 11(a) triggered reacquisition of the last shot. The graph in panel(c) in figure 11 displays the amount of reacquired data for all 14 vessel wall scans, clearly showing that the movements in patients 6 and 7 demanded reacquisition of a large part of the data. Despite this severe motion, the image quality was excellent (figure 11(b)).

Paper IV

Five plaques from patients with a transient ischemic attack (TIA) or stroke were scanned in LR SRµCT. Nine different plaque regions were imaged with 0.65 µm voxel size stitched HR SRµCT. Each stitched HR volume contained one or multiple plaque typical morphological changes. Table 12 shows details of imaging data for each plaque.

Figure 17 shows an example of the LR SRµCT of a plaque (A and B). The zoomed-in HR SRµCT images and histology in figure 17 (D-G) demonstrate an example of the interface between plaque and lumen with great visual detail. The LR SRµCT with 6.5µm voxel size allowed us to scan the entire length of the plaque and navigate in MPR. This facilitated both the sectioning process and the preliminary comparison with histology, while the final comparison was made with HR SRµCT. For the plaque in figure 17, 4x4 HR SRµCT scans were stitched, and the final result covered the entire plaque area on the axial plane. The stitching of multiple scans rendered a large area that covered multiple typical plaque features recognizable by histology but with the advantage of no tissue loss, change of plaque shape, or plaque configuration.

The following features, well known to be associated with advanced atherosclerotic plaque, were observed in SRµCT and confirmed in histology: ruptures (Fig. 18), thrombus, neo-vascularization, inflammatory infiltrates, shoulder regions with inflammatory cells, LRNC (Fig. 19), plaque-lumen interface, including the irregular endothelial surface, thin fibrous cap with varying thickness, calcifications and fragmentation of the internal elastic membrane (Fig.20). Figures of specific plaque typical pathologies are included in the manuscript IV (appendix) in the printed version of the thesis. Only a few of the examples are shown in this thesis summary.

Table 12. Imaging data

ID	Dimensions stitched LR SR µCT (pixels)	Number of stiched LR SR µCT	Dimensions stitched LR SR µCT (mm)	HR Level	Number FoV of scans	Dimensions (pixels) HR	Dimensions stitched HR SR µCT (mm)	Size (Gb)
1	4860x 2048x 2048	11	31.59x 13.26x 13.26					37.7
				1_1	4 (2x2)	2161x 4391x 4384	1.41x 2.85x 2.85	77.5
				1_2	4 (2x2)	2160x 4388x 4383	1.41x 2.85x 2.85	77.4
				1_3	4 (2x2)	2161x 4385x 4406	1.41x 2.85x 2.86	77.8
2	4860x 2048x 2048	11	31.59x 13.26x 13.26					37.7
				2_1	16 (4x4)	2162x 8052x 8037	1.41x 5.23x 5.23	260.6
				2_2	4 (2x2)	2161x 4383x 4409	1.41x 2.85x 2.87	77.8
3	1619x 2048x 2048	4	10.52x 13.26x 13.26					12.5
				3_1	1	2060x 1560x 2560	1.34x 1.01x 1.66	26.4
4	3527x 2048x 2048	8	22.93x 13.26x 13.26					27.3
				4_1	4 (2x2)	2160x 4389x 4413	1.40x 2.85x 2.86	77.9
5	4860x 2048x 2048	11	31.59x 13.26x 13.26					37.7
				5_1	4 (2x2)	2162x 4398x 4391	1.40x 2.86x 2.85	77.8
				5_2	4 (2x2)	2161 x4384 x4396	1.40x 2.85x 2.86	77.6
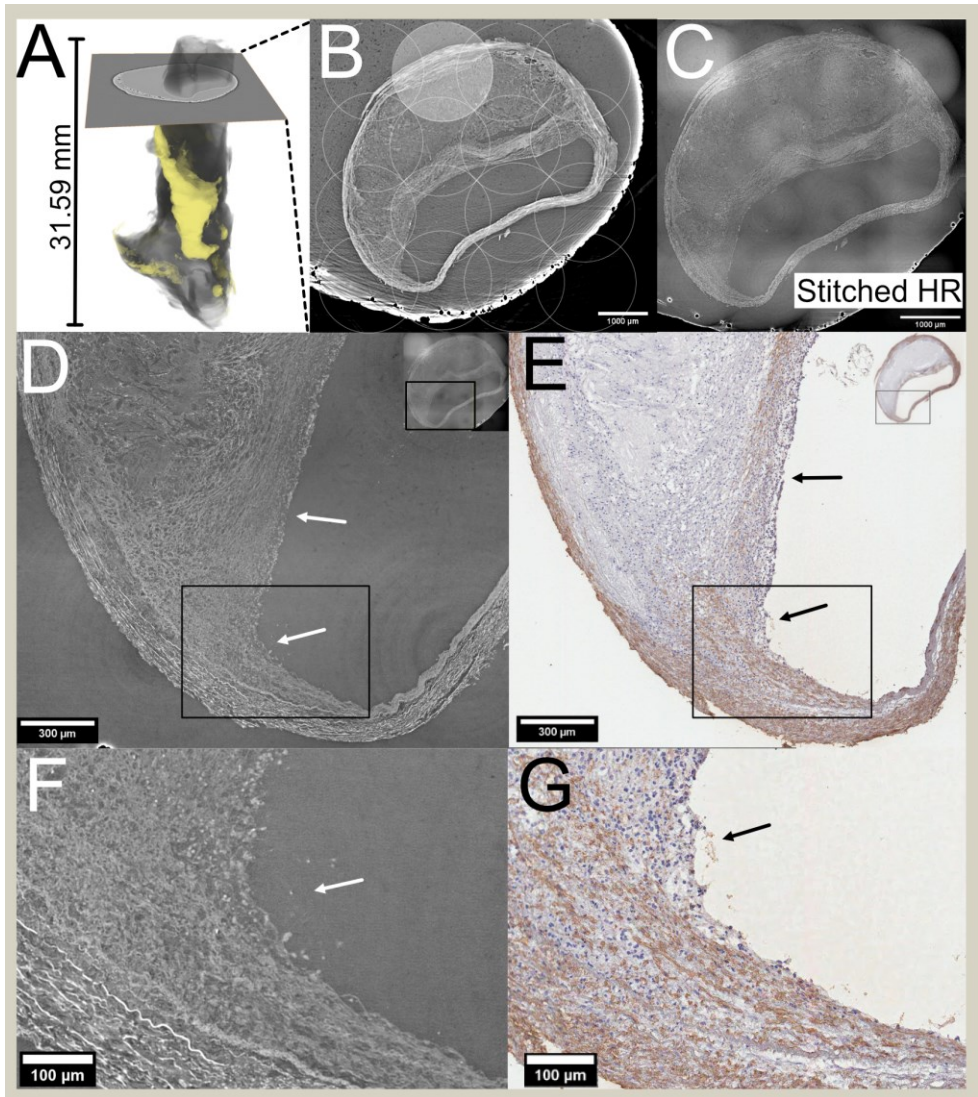
Figure 17. Low resolution (LR) and high resolution (HR) synchrotron radiation (SR) µCT with 3D rendering and histology.
(**A**) 3D volume of LR SRµCT of a sample where the cross-section represents the tomographic axial plane shown in (**B**), where the 4x4 circles indicate the tomography scans of each HR SRµCT (one highlighted, for example) that all combined, formed the final stitched volume seen in (**C**). (**D**) zoomed-in area of the plaque-lumen interface on the HR SRµCT indicated with arrows. (**F**) zoomed-in image of the area marked with a box in (D). (**E**) corresponding region stained for smooth muscle cells (alpha-actin). (**G**) the zoomed-in area within the box represented in (E).

52
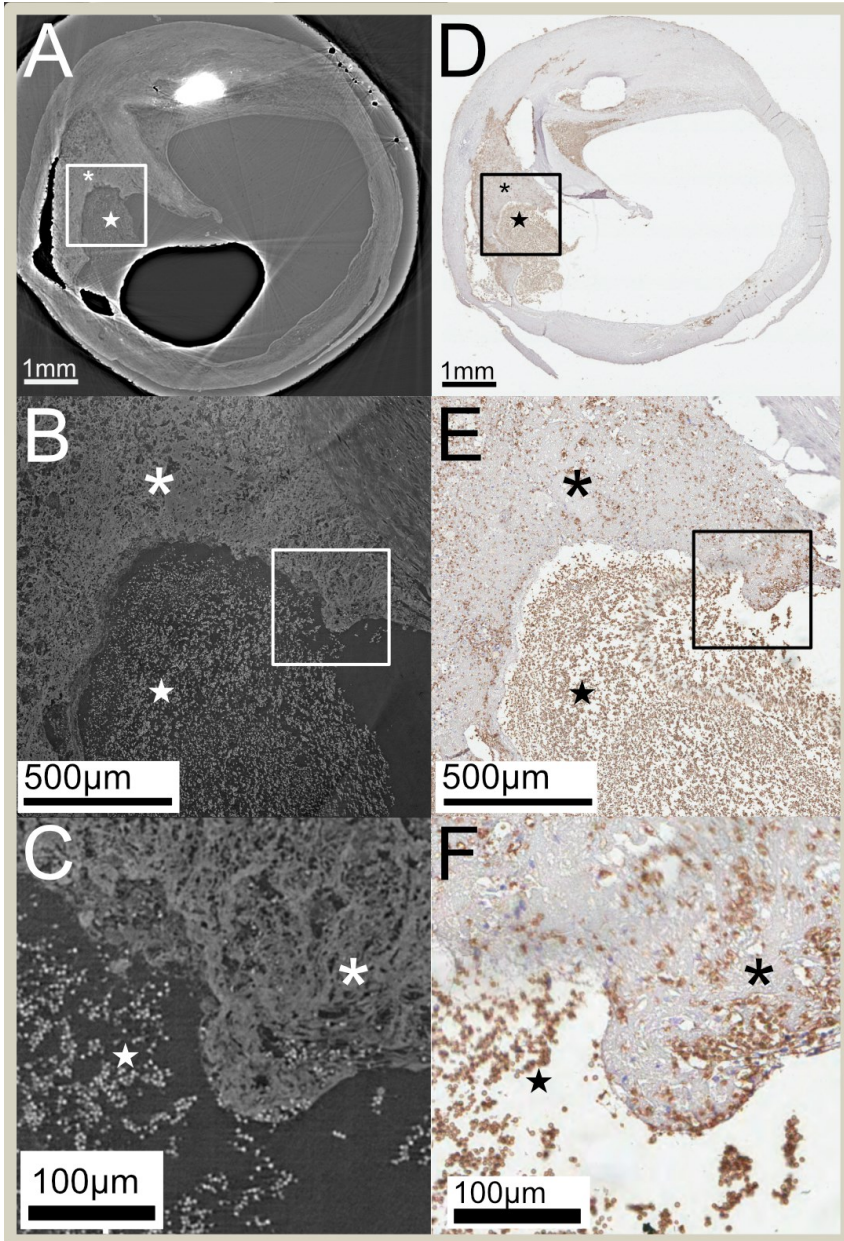
Figure 18. Rupture with plaque tissue exposed to the bloodstream with thrombus formation
(**A**) LR SRµCT of a ruptured shoulder region with plaque tissue (asterisk) exposed to the bloodstream with the formation of a thrombus (star). (**B**) the zoomed-in area of the interface between plaque tissue and thrombus, obtained with HR SRµCT. The white box in (A) corresponds to the area in (B). (**C**) shows the area with the white box in B with the zoomed-in region of the plaque tissue and thrombus interface. Individual erythrocytes are also seen scattered within the exposed plaque tissue, which is also seen in histology. The corresponding section plane in histology, stained for erythrocytes (Glycophorin A), is seen in (**D**) and zoomed in (**E**) and (**F**), where the black boxes depict the zoomed-in areas with the asterisk indicating plaque tissue and the star marking the thrombus.
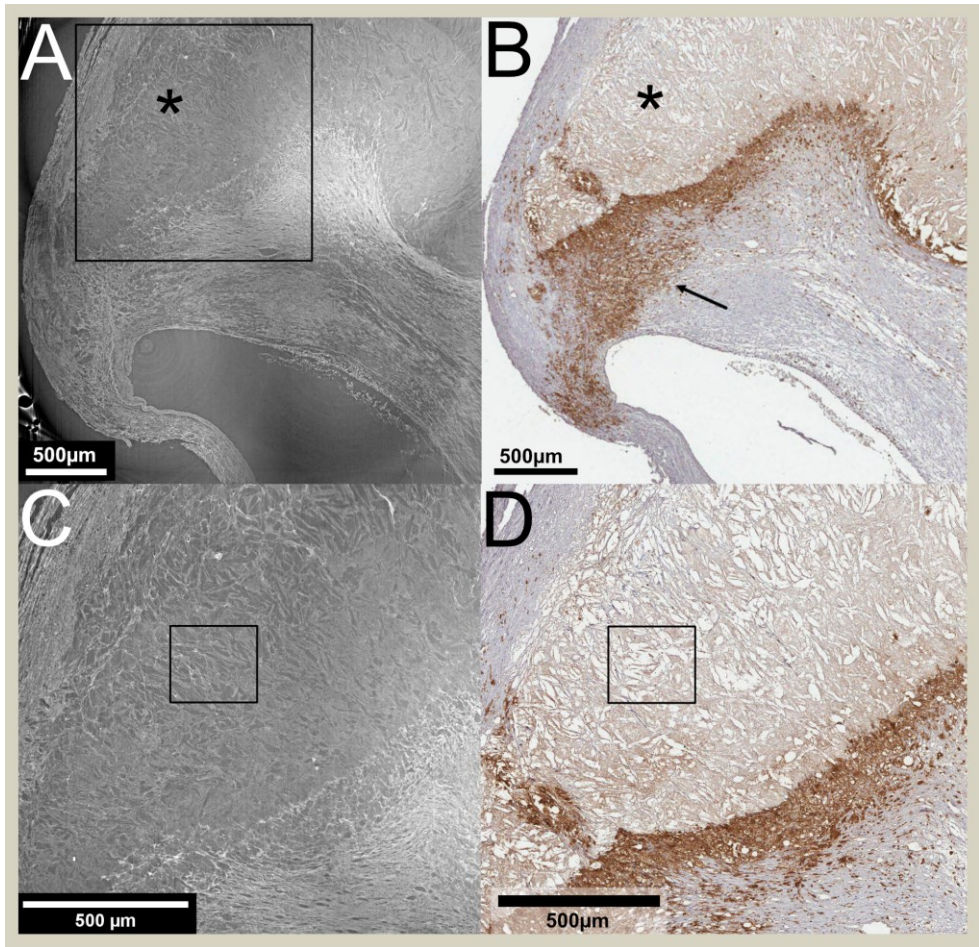
Figure 19. Plaque with lipid-rich necrotic core with cholesterol crystals
LRNC depicted with stitched HR SR µCT (**A**) and histology stained for macrophage with CD68 (**B**). A part of the LRNC is indicated with asterisks. The black arrow in (**B**) points to a region dense with macrophages. **(C)** and **(D)** are zoomed in and magnified areas representing regions rich in cholesterol crystals.
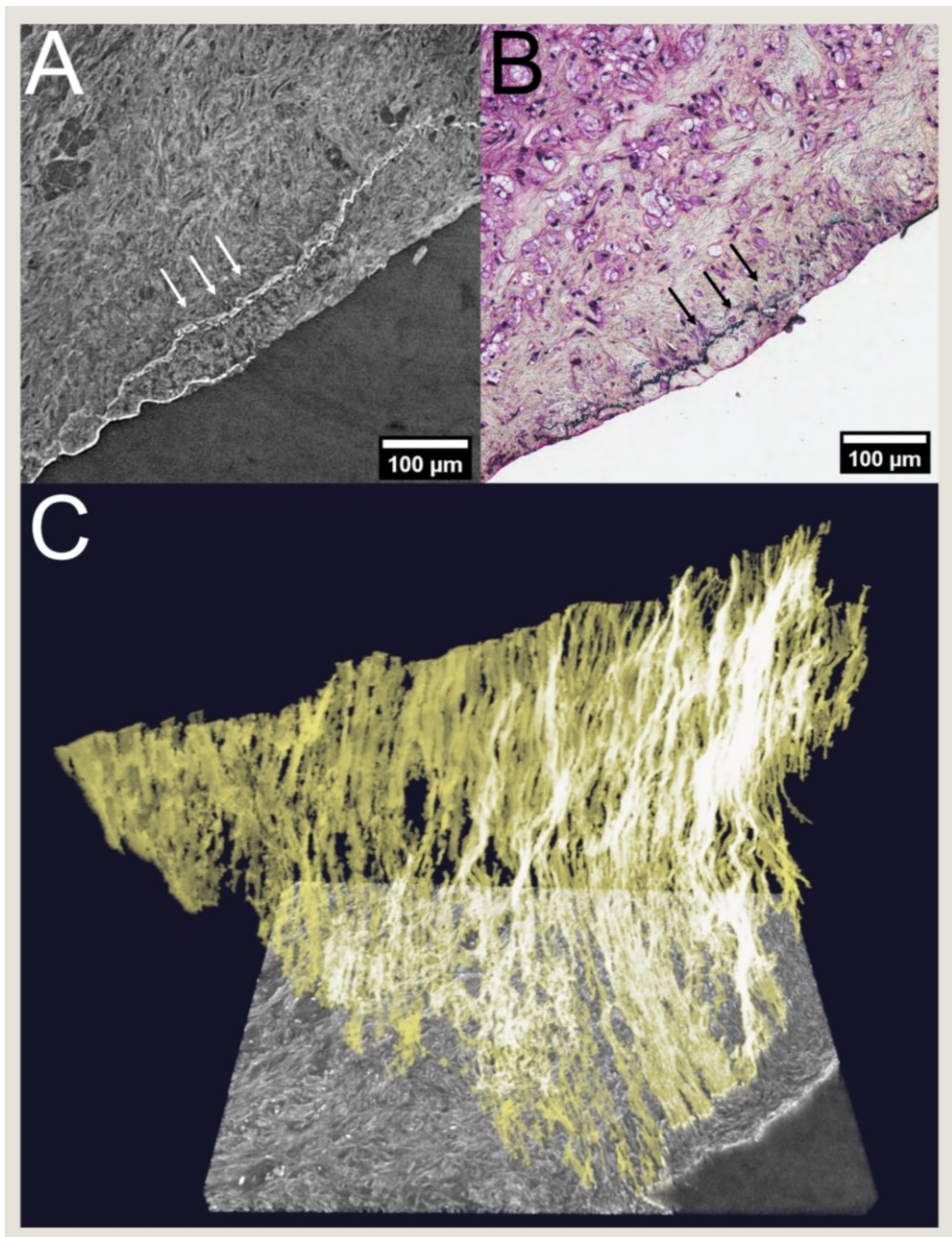
Figure 20. Internal elastic membrane depicted in 2D image stacks, histology, and 3D rendering.
HR SR µCT (**A**) and a histologic section with Movat staining (elastin in black) (**B**). The arrows indicate the internal elastic membrane. (**C**) 3D reconstruction.

Discussion

General thoughts

The Ph.D. started with *in vivo* vessel wall imaging to optimize clinical protocols. Along the path of the first research projects, there was a growing insight that carotid wall changes found on clinical imaging did not always match what was reported from surgery and quite challenging to compare with histology.

CTA and MRI study qualities of the vessel wall based on density and the paramagnetic properties of tissue, while Histology uses histochemical or immunological methods. Another factor affecting the comparison was the difference in resolution. In CT or MRI, the pixel values are at best on submillimeter levels, while in histology, resolution can range between micrometers to a couple of hundred nanometers. In paper II and paper IV, we have tried to make the difference in the resolution between radiology and histology smaller to facilitate comparison.

Imaging beyond the lumen

Decades after the large North American and European prospective randomized trials[78-81] that led to the knowledge of the association between carotid bifurcation stenosis and stroke risk, we still do not fully understand the mechanism of why some patients with atherosclerosis suffer an embolic stroke, while some patients do not (7, 31, 61, 82-84). With the emergence of more technically sophisticated clinical methods such as duplex ultrasonography, CTA, and MRI, the knowledge of stenosis derived from 2D angiograms was translated into non-invasive methods[85]. In addition to stenosis degree, blood flow, vessel wall structure, and plaque composition are also evaluated. With the development of fast multidetector computed tomography and especially after the publications of studies showing the effect of Thrombectomy[86-89], CTA of the cervical and intracranial vessels, together with NECT of the brain, has become standard diagnostics at Skåne University hospital, in acute ischemic stroke (AIS)[18].

Identification of carotid artery atherosclerosis is conventionally based on measurements of luminal stenosis and surface irregularities using *in vivo* imaging techniques, including duplex ultrasonography, CTA, MRI, and digital subtraction angiography. However, histopathologic studies demonstrate that plaques with features associated with increased risk for Stroke can show identical degrees of

stenosis as plaques with more stable features(90). The development of the non-invasive methods has been parallel (91, 92), and it has slowly shifted focus to include assessment of the vessel wall in addition to luminal stenosis. In my opinion, the development in radiology has slowly brought imaging closer to the histopathological knowledge of atherosclerosis(22, 93).

Paper I

This was an exploratory observational study to test the feasibility of a spoiled gradient-echo-based T2* weighted MRI sequence (3D MEDIC) for carotid plaque imaging and compare signs suggestive hemosiderin on 3D MEDIC with signs of methemoglobin on a T1wBB sequence.

TIA or Stroke patients were included based on the presence of non-calcified plaque components on CTA.

The degree of technical feasibility for 3D MEDIC, defined as images acceptable to both neuroradiologist readers, was 34/42 patients (81%). The poorer inter-reader agreement for 3D MEDIC than T1wBB may suggest that the image quality was inferior for the 3D MEDIC, even though both readers accepted the images. There are other possible explanations for the lower inter-reader agreement, such as the lesser experience of 3D MEDIC images.

In atherosclerotic plaques with IPH, different hemoglobin degradation products are known to co-localize(8). Intracellular methemoglobin, extracellular methemoglobin, and hemosiderin affect the signal characteristics on MRI differently(94). If the degradation products of hemoglobin co-localize, the MRI image can become complex, making IPH diagnosis challenging. Simpson et al. showed in a study with 37 patients that the elevated T1w signal was visible for two years in most cases(11).

By applying the 3D MEDIC sequence together with a T1wBB sequence, we show that non-calcified plaques contain tissue that affects susceptibility *without* simultaneous T1-shortening and that this is, in fact, a relatively common imaging feature present in 13/34 of the plaques in this group of patients. This image feature would be suggestive of hemosiderin with little or no methemoglobin. Our study also shows that an equally large group display elevated T1w signal *in combination with* a signal loss on 3D MEDIC (Table 6 and Figure 12), an imaging feature suggestive of hemosiderin and methemoglobin in combination. An alternative explanation for this finding could be the presence of tiny amounts of calcium, undetectable on CTA, which have also been demonstrated within atherosclerotic plaques(22). A recent study by Wang et al. showed co-localization of elevated T1w signal and susceptibility artifacts, like our finding, as well as the capability of quantitative susceptibility mapping to discern macro-calcifications from hemorrhage(94).

In 7/34 of the examined plaques in our study, no signal loss on 3D MEDIC or T1w-elevation was seen, which may indicate a more stable plaque composition. Lastly, we found that elevated T1w signal *without* signal loss on 3D MEDIC was an uncommon finding in this group of patients, only seen in one plaque in our study.

There are several limitations of this study. There was no histological or biochemical verification of the imaging findings, which would eventually be desired to support the hypothesis that 3D MEDIC can be used to identify hemosiderin. It is easy to overestimate the identification of plaque calcifications and signal loss in soft tissue in MRI. This could be explained by phase-encoding artifacts, resulting in a signal loss at the vessels' inner and outer edges in the phase-encoding direction. (95).

Still, we did not include histology in this study since only a small portion of the included patients were treated surgically.

Another limitation is that an SWI sequence was not included in the imaging protocol. It would be desirable to compare the technical feasibility of 3D MEDIC to SWI, even though the latter presented more artifacts in our experience, and the relationship remains to be further studied.

Paper II

This paper examined carotid plaques with a non-destructive method by imaging plaque morphology in 11.7T MRI. Since we scanned entire plaques, the image stacks served a navigational purpose and aided in the histologic process and the final comparison with histology. During sectioning in the microtome, it was not unusual for calcifications to lacerate the tissue and create artifacts and tissue loss. It could be challenging to understand the three-dimensional structure of the plaque. The MRI images were often used during the histologic process, both at the planning of section planes and to avoid large calcifications deep within the plaque.

Visual agreement of in-plane matching between histology and MRI was accomplished in all plaques in a total of 70 sections. Due to fragmentation and the fact that we did not do serial sectioning and staining on every available section, the result was 70 levels that matched between histology and MRI.

All 12 plaques contained lipids, areas with inflammation, fibrous tissue, and hemorrhage, typical of complicated symptomatic plaques. But we only included the stained sections matched with MRI for the ROI-selection process.

Our results showed that fibrous tissue and lipids could be classified based on T1 and T2* values, while it was more difficult with tissue with inflammation and hemorrhage. There was a considerable overlap of T1 and T2* values between plaques and individual components. The range was large, making it difficult to conclusively use T1 and T2* values and other ROI data for classification. However, the result for individual plaques was better.

This could indicate that the execution of the method must be more streamlined from surgery to final scan. In our project, the time interval between surgery and the scan had a considerable variation (Table 7), which could affect the results.

Paper III

This prospective study was performed to confirm previously reported findings of changes in the vessel wall following endovascular thrombectomy using 3T MRI (96-99) and to assess whether the vessel wall contrast enhancement correlates to the location of the thrombus or the stent retrievers. Furthermore, we wanted to study the use of motion correction for high-field vessel-wall MRI to compensate for patient movements.

We now report a consecutive series of 7T vessel wall imaging following successful stent retriever thrombectomy. The application of prospective motion correction in the sub-acute phase yielded excellent diagnostic images without significant motion artifacts.

Previous vessel wall imaging studies have mostly been performed on mixed treatment populations, whereas our population received the same acute stroke treatment. Power et al. reported definite vessel wall enhancement in four out of six patients treated with stent retriever thrombectomy, with possible enhancement in the remaining two(99). However, Seo et al. reported vessel wall enhancement in only five out of nine patients treated with single-pass stent retriever thrombectomy(96). In the present study, we found consistent vessel wall enhancement in all seven patients, possibly owing to the increased signal-to-noise ratio at 7T compared to 3T and the use of prospective motion correction to mitigate motion artifacts. We also established that vessel wall enhancement in all cases correlated with the deployment zone of the stent retriever rather than the location of the lodged embolus. It is known that endovascular procedures on intracranial blood vessels, such as aneurysm coiling, can result in vessel wall contrast enhancement(100), and mechanical interference to the vessel wall during stent retriever thrombectomy could potentially be extensive since the over-sized stent is deployed and retracted along extensive parts of the affected vessel. Thus, vessel wall contrast enhancement seems to be the normal state following stent retriever thrombectomy, and we can see that better, using 7T MRI with prospective motion correction.

Recently, specialized black blood sequences at 7T MR have yielded high-resolution vessel wall images(27, 51, 52, 101, 102). Direct comparisons demonstrate that 7T images reveal more vessel wall lesions than a 3T examination and that the vessel walls also display a higher contrast to the surrounding tissue(26). Validations of wall thickness measurements have been performed by comparing MRI imaging of *ex vivo* specimens to histological measurements(54).

In our series of seven patients, image quality was independently rated excellent by two experienced neuroradiologists. With the use of a novel prospective motion correction technique (iMOCO), neither of the reviewers noted that motion artifacts impaired the diagnostic quality, despite severe motion in some cases. This contrasts with the study by Harteveld et al.(26), where prospective motion correction was not used, and motion artifacts hampered assessment in several cases.

It was not possible to obtain quantitative flow data in three of the subjects due to unreliable cardiac triggering. For the four patients where flow data were obtained, no significant differences in flow parameters could be seen between the treated and untreated sides, which is expected with a complete restoration of normal blood supply.

The small number of subjects limits this study, and future studies with larger study groups are warranted to support our findings. Furthermore, longitudinal studies would be desirable to determine how long vessel wall enhancement is sustained.

Paper IV

This concept study demonstrates that synchrotron radiation µCT results in excellent microscopic resolution of human carotid atherosclerotic plaques. This non-destructive method provides tomographic 3D datasets with low resolution (6.5 µm) and high resolution (0.65 µm) voxel sizes and excellent tissue contrast with the Paganin phase retrieval method. We studied five plaques and obtained images of multiple typical plaque features, including ruptures, thrombus, neo-vascularization, inflammatory infiltrates, shoulder regions, LRNC, disrupted endothelium at the plaque-lumen interface, thin fibrous caps, calcifications, lumen irregularities, and internal elastic membrane fragmentation. The HR SRµCT was of such high resolution that comparison with histology and analysis of microstructures were possible.

The non-destructive nature of whole plaque synchrotron radiation-based µCT allows carotid plaque visualization with preserved integrity of the three-dimensionality of complex structures that are difficult to appreciate by 2D histology images. Complex pathological features such as ruptures, thrombi, LRNC, luminal irregularities, and the internal elastic membrane can be viewed in any plane and are readily visualized with 3D rendering.

Histological and immunohistochemical methods are regarded as the gold standard to analyze plaque tissue *ex vivo* and provide much information about plaque morphology. Still, the mechanically and chemically destructive preparation process necessary to obtain histological images may compromise the integrity and composition and potentially confound the interpretation of the tissue specimen. A non-destructive method such as SRµCT that allows multiple re-scans can

complement histology to mitigate such processing-induced artifacts and help understand plaque histopathology.

The possibility of analysis in MPR and 3D advances the perception and understanding of typical plaque structures.

For our study, we used the established Paganin phase-retrieval method(67) that rendered excellent contrast in all plaque areas except in proximity to large calcifications or air bubbles entrapped in the paraffin embedding medium.

Imaging of human carotid plaques with SRµCT can bridge the resolution gap between clinical CT and histology and advance the understanding and interpretation of clinical CT. In general, applying a non-destructive method such as SRµCT makes it easier to translate histopathological findings into CT images. The technique can potentially also help us interpret CT findings in a clinical setting, in multiple organ systems and pathologies.

Imaging with Synchrotron µCT in TOMCAT allowed us to go from an overview scale of the entire plaque to a scale that allowed us to study details in morphology. The two-step method to navigate the 3D volume of the plaque facilitated comparison with histology, both before sectioning and after sectioning. The LR acquisition allowed the assessment of overall plaque geometry due to its FoV, thus being able to look at changes of the whole plaque, such as lumen irregularities, the bulging shape of the exocentric plaque growth, the variations of the luminal stenosis, and the general size of the plaque in multiple planes. In addition, the HR part of the µCT allowed details in plaque ruptures, neo-vasculature, individual erythrocytes, cholesterol crystals in lipid-rich necrotic cores to be visualized with a high level of detail. The high resolution also made it possible to create high-quality segmented 3D renderings of the different plaque structures. In this paper, the 3D segmentation of the internal elastic revealed a pathological perforated composition.

As long as the plaque was mounted and not moved, the setup at the TOMCAT allowed for a fast switch between LR and HR images, and evaluation and selection of areas of interest found on LR could easily be examined with the HR setting.

The strength with synchrotron-based µCT compare to lab-based µCT is the possibility of higher resolution in combination with higher scan speed and with very high contrast. In our study, the voxels with the highest resolution were 0,65µm, and it was possible to discriminate individual red blood cells. Because of the fast scan time, multiple adjacent scans were possible, and hence final stitched FOV could be enlarged, and total scan time could still be counted in minutes. In a lab-based µCT, the same scan would take at least a full day, and the contrast would still not reach the same quality.

Histology

In this paper, as well as in paper II, histology played a central part. When handling the atherosclerotic plaque, some circumstances make it harder to process the tissue. The overall structure of the plaque during sectioning can be distorted or lacerated. Depending on plaque structure and composition, fragmentation and laceration are common, leading to loss of information.

Calcifications generally pose practical problems in histology, especially during sectioning. Commonly, tissues lacerate, and large calcifications become fragmented as well as dislodged. In synchrotron phase-contrast µCT, macro-calcifications can also cause problems since they absorb more radiation than surrounding non-calcified tissue, leading to artifacts, especially at the interface between calcifications and the surrounding soft tissue as well as an oversaturated image of the calcification. Calcifications can still be visualized to some extent by adapting the dynamic range to very dense tissue.

Beam starvation artifacts are less of a problem in sites with small calcifications, which allow us to image the distribution and morphological layout of microcalcifications. The distribution of microcalcifications was overall consistent between SRµCT and histology, but even small calcifications could be seen dislodged in histology from their original position in the tissue. In situations where the calcifications had moved outside of the main plaque section, the disruption of original morphology was apparent. But, in histologic sections where the microcalcifications had moved within plaque margins, the change was less noticeable and better seen when compared to the congruent axial plane on HR SRµCT.

Conclusions

This thesis shows that *in vivo* and *ex vivo* radiologic imaging enhances our understanding of vessel wall changes and microstructures in carotid plaques. The following conclusions can be drawn from the individual papers:

Paper I

- High-resolution plaque imaging using 3D MEDIC is feasible in most patients.

- Combining a T1w sequence and the 3D MEDIC might be a tool to identify the different hemoglobin degradation products, but future studies where histology is included are needed.

- MEDIC could potentially expand the diagnostic window to diagnose intraplaque hemorrhage since hemosiderin stays longer in tissue than methemoglobin.

Paper II

- 11.7T *ex vivo* high-resolution MRI shows good visual agreement with histology in carotid plaques.

- MRI with T1/T2* maps analyzed with QDA is a promising non-destructive method to classify plaque content, especially fibrous tissue and lipids. The classification is more challenging in the presence of hemorrhage or inflammation.

Paper III

- *In vivo* 7T vessel wall MRI with prospective motion correction following endovascular thrombectomy is a safe and reliable method to image the arterial wall of the middle cerebral artery.

- Gadolinium uptake in the arterial wall is the normal post-operative state following stent retriever thrombectomy and corresponds with the deployment zone of the stent retriever.

- Prospective motion correction was useful in mitigating motion artifacts even though some patients moved considerably during the examination.

Paper IV

- Synchrotron radiation-based phase-contrast μCT with submicron voxel size is an excellent non-destructive method to image clinically relevant features of the atherosclerotic plaques.

- The method gives high resolution, multiplanar 2D and 3D images of microstructures that are easy to compare to histology visually. We could identify and analyze detailed plaque-typical pathological structures, such as rupture, thrombus, neo-vessels, LRNC, and structural changes of the internal elastic membrane.

Future perspectives

In vivo vessel wall imaging can be a challenge to apply in a clinical setting, primarily due to limitations in available machine time. The need for a subacute carotid vessel wall MRI depends on the characteristics of the carotid plaque found on CTA and duplex ultrasonography. In my opinion, plaques with moderate stenosis in young patients or plaques that are difficult to study with ultrasonography could be further investigated with MRI. Since the value of carotid MRI in TIA and stroke has not been studied in large, prospective, randomized studies, the need for the exam should, in my opinion, be individually assessed by the radiologist together with the clinician.

In paper III, we showed that vessel wall imaging in 7T MRI gave high-quality images, and the application of high-field MRI of intracranial vessels is promising. In vasculitis and other lesions that affect intracranial arteries, 7T MRI is a good tool for future vessel wall research, especially if motion correction software is applied.

In paper IV, further questions were raised concerning the microstructural composition of plaque tissue. Tissue density and phase contrast could not always differentiate between scattered micro-calcifications and multiple cells projected on top of each other, especially in areas with co-localization. In the TOMCAT data, we also encountered structures that histology revealed as iron, co-localizing with calcifications. These findings led us to a separate study with synchrotron-based X-ray fluorescence at the MAX IV facility in Lund, allowing us to quantify elements such as iron and calcium. The method gave us " element maps" with exact quantification of iron and calcium in tissue on a microscopic level (nanometer resolution). The element maps of iron and calcium were compared to density-based X-ray images. The data is still under analysis and not yet published, but the preliminary results offer a new horizon to atherosclerotic research.

Sammanfattning på svenska

Stroke, eller slaganfall, är en allvarlig sjukdom där vanligaste orsaken är en blodpropp som stoppar blodtillförseln till hjärnan, vilket leder till hjärninfarkt. De flesta proppar kommer från hjärtat, men en stor del kommer även från åderförkalkning i främre halspulsådern. En del patienter får övergående strokesymptom. Detta kallas för transitorisk ischemisk attack (TIA) som är ett varningstecken för förestående stroke.

På senare år har Strokevården förbättrats markant, med snabbare handläggning och revolutionerande behandlingar som Trombektomi, en operation, där man genom ett stick i ljumsken går in i artärerna och via plastslangar och vajrar, drar ut proppen.

Handläggningen av TIA och stroke, innefattar skyndsam avbildning av artärer och blodförsörjning till hjärnan, vilket görs med ultraljud, datortomografisk angiografi (CTA) samt ibland magnetresonanstomografi (MR).

Mycket kunskap om artärer och åderförkalkning kommer från histopatologi, läran om sjukliga förändringar i vävnader. Vävnad erhållna från avlidna eller sotningsoperationer i halspulsådern har studerats med histopatologiska metoder där man tittar på vävnaden i mikroskop. För att studera åderförkalkning i mikroskop måste vävnaden förberedas med snittning och infärgningar. Detta kan göra det svårare att i efterhand förstå plackets sammansättning och form, när det befann sig i kroppen. I vår digitala era sparas mikroskopibilder i digital form och i denna avhandling har vi bland annat jämfört radiologiska bilder med digitala mikroskopibilder.

I tre av avhandlingens arbeten har vi undersökt åderförkalkning i främre halspulsådern, både innan den opererats ut och efter operation. I ett av arbetena har vi tittat på kärlväggsförändringar i hjärnans artärer, efter en trombektomi. Genom dessa arbeten har vi försökt att göra det lättare att tolka radiologiska bilder utifrån den histopatologiska kunskapsbasen.

I det första arbetet studerade vi åderförkalkningsplack i främre-halspulsådern, med magnetisk resonanstomografi. Då andra forskare har visat att blödning i åderförkalkning kan vara kopplat till slaganfall, ville vi studera placken med en ny MR-metod, för att hitta tecken på äldre blödningar. Vi undersökte patienter med stroke eller TIA som hade genomgått en datortomografisk kärlröntgen, en CTA, för att kunna skilja mellan förkalkad och icke-förkalkad plaquevävnad (där det kan

finnas blodrester) och jämförde de icke-förkalkade delarna med MR undersökningen. Våra resultat visade att mer än en tredjedel hade vävnadsegenskaper som kunde tala för gammalt blod. Vi hade dock inte jämfört med histologi och kunde inte vara helt säkra i vår slutsats.

I det andra pappret undersökte vi tolv oskurna åderförkalkningsplack i en labbkamera med extremt starkt magnetfält som gav oss MR-bilder med mikroskopisk bildupplösning. Dessa jämförde vi med histologiska bilder av samma plaque och försökte utvärdera om en viss MR-teknik tillsammans med matematiska beräkningar, kunde skilja på olika komponenter i placket. Vi kom fram till att det gick bra att särskilja områden med fett eller bindväv, medan inflammation och blödningsrester var svårare.

I det tredje arbetet, avbildade vi kärlväggen i hjärnans artärer i 7T MR, med rörelsekorrigeringsprogram. 7T MR är en kamera med det starkaste magnetfältet som används på människor i Sverige. Detta gjorde det möjligt att få högupplösta bilder av kärlväggsförändringar som visade sig vara orsakade av instrumenten som används i trombektomi. Dessa förändringar är sannolikt övergående och i sammanhanget mindre viktiga, men studien var relevant för att utvärdera en säker metod att avbilda hjärnans artärer i 7T MR.

I det fjärde pappret, studerade vi åderförkalkningsplack med mikroskopisk datortomografi (μCT) där vi använde röntgenstrålning från en synkrotron, en partikelaccelerator. Synkrotronljus kan avbilda oskuren vävnad på mikroskopisk nivå. Efter μCT bereddes placken histologiskt och därefter jämförde vi bilderna från μCT med histologin. Det visade sig att μCT kunde identifiera många olika områden djupt inne i åderförkalkningen. Man fick även förståelse för vävnadens tredimensionella utformning.

Sammanfattningsvis har vi undersökt halspulsåder-åderförkalkning samt hjärnartärer med olika typer av CT och MR, för att få så detaljerade bilder som möjligt. Den höga upplösningen underlättar jämförelsen med histologi, vilket i förlängningen kan leda oss till bättre tolkningar av röntgenbilder i den kliniska vardagen.

Acknowledgments

During my Ph.D., I have had the privilege and opportunity to work with fellow researchers from vastly different fields. This has brought me valuable knowledge and insight into the research process that I will gratefully cherish.

Many people have helped me during my work with this thesis, and I thank you all!

I would like to thank my supervisors:

Johan Wasselius, my principal supervisor. You helped me streamline my hypothesis and provided resources, guidance and support to complete my thesis. Thank you for a mean machine research computer with computational power to make a teenage gamer envious.

Isabel Goncalves introduced me to atherosclerotic research and provided many means and resources. Having breakfast together with you and Till Dreier, at the Frei café in Brugge, after a memorable and food-deprived beam time, was one of the highlights of my Ph.D.

Karin Markenroth Bloch, thank you for introducing me to the possibilities of 7T MRI. One of the best things about working in Lund is the proximity to great physicists like you.

Roger Siemund, thank you for encouraging me to start a Ph.D. and for helping to set up MRI vessel wall imaging in BoF.

In addition to my supervisors, many others have helped me.

I especially would like to thank all my other co-authors. This thesis would not have been possible without your help and contribution. Thank you, *Adnan Bibic, Rene In't Zandt, Lena Sundius, Ana Persson, Makda HaileMichael, Martin Bech, Till Dreier, Jonas Svensson, Jimmy Lätt, Johannes Töger, Mads Andersen, Gunnar Andsberg, Anne Bonnin, Goran Lovric, Finn Lennartsson and Claes Håkansson.*

In memory of *Professor Peter Höglund*. Thank you for your contribution to the method and statistics in paper II. Academia has lost a champion.

To professor *Pia Maly-Sundgren*, Department of Diagnostic Radiology, thank you for your support during my Ph.D.

Financial support

References

1. J. Cai *et al.*, In vivo quantitative measurement of intact fibrous cap and lipid-rich necrotic core size in atherosclerotic carotid plaque: comparison of high-resolution, contrast-enhanced magnetic resonance imaging and histology. *Circulation* **112**, 3437-3444 (2005).

2. J. M. Cai *et al.*, Classification of human carotid atherosclerotic lesions with in vivo multicontrast magnetic resonance imaging. *Circulation* **106**, 1368-1373 (2002).

3. T. Saam *et al.*, Prevalence of American Heart Association type VI carotid atherosclerotic lesions identified by magnetic resonance imaging for different levels of stenosis as measured by duplex ultrasound. *Journal of the American College of Cardiology* **51**, 1014-1021 (2008).

4. C. Yuan *et al.*, Contrast-enhanced high resolution MRI for atherosclerotic carotid artery tissue characterization. *Journal of magnetic resonance imaging : JMRI* **15**, 62-67 (2002).

5. X. Zhao *et al.*, Discriminating carotid atherosclerotic lesion severity by luminal stenosis and plaque burden: a comparison utilizing high-resolution magnetic resonance imaging at 3.0 Tesla. *Stroke; a journal of cerebral circulation* **42**, 347-353 (2011).

6. F. Li *et al.*, Scan-rescan reproducibility of carotid atherosclerotic plaque morphology and tissue composition measurements using multicontrast MRI at 3T. *Journal of magnetic resonance imaging : JMRI* **31**, 168-176 (2010).

7. H. R. Underhill, T. S. Hatsukami, Z. A. Fayad, V. Fuster, C. Yuan, MRI of carotid atherosclerosis: clinical implications and future directions. *Nature reviews. Cardiology* **7**, 165-173 (2010).

8. W. J. Derksen *et al.*, Different stages of intraplaque hemorrhage are associated with different plaque phenotypes: a large histopathological study in 794 carotid and 276 femoral endarterectomy specimens. *Atherosclerosis* **218**, 369-377 (2011).

9. A. A. Hosseini, N. Kandiyil, S. T. Macsweeney, N. Altaf, D. P. Auer, Carotid plaque hemorrhage on magnetic resonance imaging strongly predicts recurrent ischemia and stroke. *Annals of neurology* **73**, 774-784 (2013).

10. A. A. Hosseini *et al.*, Magnetic Resonance Imaging Plaque Hemorrhage for Risk Stratification in Carotid Artery Disease With Moderate Risk Under Current Medical Therapy. *Stroke; a journal of cerebral circulation* **48**, 678-685 (2017).

11. R. J. Simpson *et al.*, MR imaging-detected carotid plaque hemorrhage is stable for 2 years and a marker for stenosis progression. *AJNR. American journal of neuroradiology* **36**, 1171-1175 (2015).

12. H. Chen, Q. Zhang, W. Kerwin, Analysis of Multicontrast Carotid Plaque MR Imaging. *Neuroimaging Clin N Am* **26**, 13-28 (2016).

13. B. Chu *et al.*, Hemorrhage in the atherosclerotic carotid plaque: a high-resolution MRI study. *Stroke; a journal of cerebral circulation* **35**, 1079-1084 (2004).

14. W. S. Kerwin, Carotid artery disease and stroke: assessing risk with vessel wall MRI. *ISRN cardiology* **2012**, 180710 (2012).

15. C. Yuan *et al.*, In vivo accuracy of multispectral magnetic resonance imaging for identifying lipid-rich necrotic cores and intraplaque hemorrhage in advanced human carotid plaques. *Circulation* **104**, 2051-2056 (2001).

16. A. R. Moody, N. Singh, Incorporating Carotid Plaque Imaging into Routine Clinical Carotid Magnetic Resonance Angiography. *Neuroimaging Clinics of North America* **26**, 29-44 (2016).

17. R. E. Murphy *et al.*, Prevalence of complicated carotid atheroma as detected by magnetic resonance direct thrombus imaging in patients with suspected carotid artery stenosis and previous acute cerebral ischemia. *Circulation* **107**, 3053-3058 (2003).

18. SBU (2021) Vetenskapligt underlag till Socialstyrelsens nationella riktlinjer för strokesjukvård.

19. J. M. Wardlaw, F. M. Chappell, J. J. Best, K. Wartolowska, E. Berry, Non-invasive imaging compared with intra-arterial angiography in the diagnosis of symptomatic carotid stenosis: a meta-analysis. *Lancet (London, England)* **367**, 1503-1512 (2006).

20. H. Chen, Q. Zhang, W. Kerwin, Analysis of Multicontrast Carotid Plaque MR Imaging. *Neuroimaging Clinics of North America* **26**, 13-28 (2016).

21. J. B. Michel, R. Virmani, E. Arbustini, G. Pasterkamp, Intraplaque haemorrhages as the trigger of plaque vulnerability. *European heart journal* **32**, 1977-1985, 1985a, 1985b, 1985c (2011).

22. J. N. Redgrave, J. K. Lovett, P. J. Gallagher, P. M. Rothwell, Histological assessment of 526 symptomatic carotid plaques in relation to the nature and timing of ischemic symptoms: the Oxford plaque study. *Circulation* **113**, 2320-2328 (2006).

23. L. Dong *et al.*, Geometric and compositional appearance of atheroma in an angiographically normal carotid artery in patients with atherosclerosis. *AJNR. American journal of neuroradiology* **31**, 311-316 (2010).

24. L. J. De Cocker *et al.*, Clinical vascular imaging in the brain at 7T. *NeuroImage* 10.1016/j.neuroimage.2016.11.044 (2016).

25. N. Dieleman *et al.*, Imaging intracranial vessel wall pathology with magnetic resonance imaging: current prospects and future directions. *Circulation* **130**, 192-201 (2014).

26. A. A. Harteveld *et al.*, High-resolution intracranial vessel wall MRI in an elderly asymptomatic population: comparison of 3T and 7T. *European radiology* **27**, 1585-1595 (2017).

27. A. A. Harteveld *et al.*, Detecting Intracranial Vessel Wall Lesions With 7T-Magnetic Resonance Imaging: Patients With Posterior Circulation Ischemia Versus Healthy Controls. *Stroke; a journal of cerebral circulation* **48**, 2601-2604 (2017).

28. A. L. Mescher, *Junqueira's basic histology : text and atlas* (2018).

29. A. P. Seth Love, James Ironside, Herbert Budka, *Greenfield's Neuropathology* (2015), vol. 1.

30. R. S. Henry George Liddel (pp A Gree-English online lexicon.

31. P. Libby *et al.*, Atherosclerosis. *Nature Reviews Disease Primers* **5**, 56 (2019).

32. V. L. Feigin, B. Norrving, G. A. Mensah, Global Burden of Stroke. *Circulation research* **120**, 439-448 (2017).

33. A. G. Thrift *et al.*, Global stroke statistics. *International journal of stroke : official journal of the International Stroke Society* **12**, 13-32 (2017).

34. W. H. Organization (in *World Health Organization (WHO). The atlas of heart disease and stroke.*, ed W. h. o. (WHO).

35. M. Katan, A. Luft, Global Burden of Stroke. *Seminars in neurology* **38**, 208-211 (2018).

36. M. L. Flaherty *et al.*, Carotid artery stenosis as a cause of stroke. *Neuroepidemiology* **40**, 36-41 (2013).

37. H. El Aidi *et al.*, Cross-sectional, prospective study of MRI reproducibility in the assessment of plaque burden of the carotid arteries and aorta. *Nat Clin Pract Cardiovasc Med* **6**, 219-228 (2009).

38. I. Kallikazaros, C. Tsioufis, S. Sideris, C. Stefanadis, P. Toutouzas, Carotid Artery Disease as a Marker for the Presence of Severe Coronary Artery Disease in Patients Evaluated for Chest Pain. *Stroke; a journal of cerebral circulation* **30**, 1002-1007 (1999).

39. N. Kajitani *et al.*, Chronic kidney disease is associated with carotid atherosclerosis and symptomatic ischaemic stroke. *J Int Med Res* **46**, 3873-3883 (2018).

40. T. Saam *et al.*, Quantitative evaluation of carotid plaque composition by in vivo MRI. *Arteriosclerosis, thrombosis, and vascular biology* **25**, 234-239 (2005).

41. T. Saam *et al.*, Meta-analysis and systematic review of the predictive value of carotid plaque hemorrhage on cerebrovascular events by magnetic resonance imaging. *Journal of the American College of Cardiology* **62**, 1081-1091 (2013).

42. M. M. Mughal *et al.*, Symptomatic and asymptomatic carotid artery plaque. *Expert review of cardiovascular therapy* **9**, 1315-1330 (2011).

43. T. M. Freilinger *et al.*, Prevalence of nonstenosing, complicated atherosclerotic plaques in cryptogenic stroke. *JACC. Cardiovascular imaging* **5**, 397-405 (2012).

44. A. Kampschulte *et al.*, Differentiation of intraplaque versus juxtaluminal hemorrhage/thrombus in advanced human carotid atherosclerotic lesions by in vivo magnetic resonance imaging. *Circulation* **110**, 3239-3244 (2004).

45. X. Zhao *et al.*, Prevalence and Characteristics of Carotid Artery High-Risk Atherosclerotic Plaques in Chinese Patients With Cerebrovascular Symptoms: A Chinese Atherosclerosis Risk Evaluation II Study. *Journal of the American Heart Association* **6** (2017).

46. J. Sun, T. S. Hatsukami, Plaque Imaging to Decide on Optimal Treatment: Medical Versus Carotid Endarterectomy Versus Carotid Artery Stenting. *Neuroimaging Clinics of North America* **26**, 165-173 (2016).

47. J. Sun *et al.*, Carotid Plaque Lipid Content and Fibrous Cap Status Predict Systemic CV Outcomes: The MRI Substudy in AIM-HIGH. *JACC. Cardiovascular imaging* **10**, 241-249 (2017).

48. D. Bos *et al.*, Atherosclerotic Carotid Plaque Composition and Incident Stroke and Coronary Events. *Journal of the American College of Cardiology* **77**, 1426-1435 (2021).

49. W. Koning *et al.*, MRI of the carotid artery at 7 Tesla: quantitative comparison with 3 Tesla. *Journal of magnetic resonance imaging : JMRI* **41**, 773-780 (2015).

50. A. G. van der Kolk *et al.*, Imaging the intracranial atherosclerotic vessel wall using 7T MRI: initial comparison with histopathology. *AJNR. American journal of neuroradiology* **36**, 694-701 (2015).

51. A. G. van der Kolk *et al.*, Intracranial vessel wall imaging at 7.0-T MRI. *Stroke; a journal of cerebral circulation* **42**, 2478-2484 (2011).

52. A. G. van der Kolk *et al.*, Multi-sequence whole-brain intracranial vessel wall imaging at 7.0 tesla. *European radiology* **23**, 2996-3004 (2013).

53. A. A. Harteveld, N. P. Denswil, Quantitative Intracranial Atherosclerotic Plaque Characterization at 7T MRI: An Ex Vivo Study with Histologic Validation. **37**, 802-810 (2016).

54. A. A. Harteveld *et al.*, Ex vivo vessel wall thickness measurements of the human circle of Willis using 7T MRI. *Atherosclerosis* **273**, 106-114 (2018).

55. M. Lhuaire *et al.*, Human developmental anatomy: Microscopic magnetic resonance imaging (μMRI) of four human embryos (from Carnegie Stage 10 to 20). *Annals of Anatomy - Anatomischer Anzeiger* **196**, 402-409 (2014).

56. B. R. Smith, E. Linney, D. S. Huff, G. A. Johnson, Magnetic resonance microscopy of embryos. *Computerized Medical Imaging and Graphics* **20**, 483-490 (1996).

57. D. Stucht *et al.*, Highest Resolution In Vivo Human Brain MRI Using Prospective Motion Correction. *PloS one* **10**, e0133921 (2015).

58. J. Budde, G. Shajan, K. Scheffler, R. Pohmann, Ultra-high resolution imaging of the human brain using acquisition-weighted imaging at 9.4T. *NeuroImage* **86**, 592-598 (2014).

59. A. J. Taylor, M. Salerno, R. Dharmakumar, M. Jerosch-Herold, T1 Mapping: Basic Techniques and Clinical Applications. *JACC: Cardiovascular Imaging* **9**, 67-81 (2016).

60. V. Puntmann, A. Zeiher, E. Nagel, T1 and T2 mapping in myocarditis: seeing beyond the horizon of Lake Louise Criteria and histopathology. *Expert review of cardiovascular therapy* **16** (2018).

61. B. F. Coolen *et al.*, Vessel wall characterization using quantitative MRI: what's in a number? *Magma* 10.1007/s10334-017-0644-x (2017).

62. B. F. Coolen *et al.*, Three-dimensional quantitative T1 and T2 mapping of the carotid artery: Sequence design and in vivo feasibility. *Magnetic resonance in medicine* **75**, 1008-1017 (2016).

63. B. Forkman, *Och det blev ljus : hur MAX-lab kom till, växte upp och blev stort* (Avd. för idé- och lärdomshistoria, Univ., Lund :, 2001).

64. F. Fusseis, X. Xiao, C. Schrank, F. De Carlo, A brief guide to synchrotron radiation-based microtomography in (structural) geology and rock mechanics. *Journal of Structural Geology* **65**, 1-16 (2014).

65. A. Miettinen, I. V. Oikonomidis, A. Bonnin, M. Stampanoni, NRStitcher: non-rigid stitching of terapixel-scale volumetric images. *Bioinformatics* **35**, 5290-5297 (2019).

66. H. Dejea *et al.*, Comprehensive Analysis of Animal Models of Cardiovascular Disease using Multiscale X-Ray Phase Contrast Tomography. *Scientific reports* **9**, 6996 (2019).

67. D. Paganin, S. C. Mayo, T. E. Gureyev, P. R. Miller, S. W. Wilkins, Simultaneous phase and amplitude extraction from a single defocused image of a homogeneous object. *J Microsc* **206**, 33-40 (2002).

68. H. Hillman, Limitations of clinical and biological histology. *Med Hypotheses* **54**, 553-564 (2000).

69. E. Weeks.

70. O. Ghekiere *et al.*, Image quality in coronary CT angiography: challenges and technical solutions. *Br J Radiol* **90**, 20160567 (2017).

71. J. T. Bushberg, *The essential physics of medical imaging* (Wolters Kluwer / Lippincott Williams & Wilkins, Philadelphia, PA, 2012).

72. Gareth James, Daniela Witten, Trevor Hastie, Robert Tibshirani, *An introduction to statistical learning : with applications in R* (New York : Springer, [2013] ©2013, 2013).

73. M. Andersen, I. M. Björkman-Burtscher, A. Marsman, E. T. Petersen, V. O. Boer, Improvement in diagnostic quality of structural and angiographic MRI of the brain using motion correction with interleaved, volumetric navigators. *PloS one* **14**, e0217145 (2019).

74. D. Gallichan, J. P. Marques, R. Gruetter, Retrospective correction of involuntary microscopic head movement using highly accelerated fat image navigators (3D FatNavs) at 7T. *Magnetic resonance in medicine* **75**, 1030-1039 (2016).

75. M. D. Tisdall *et al.*, Volumetric navigators for prospective motion correction and selective reacquisition in neuroanatomical MRI. *Magnetic resonance in medicine* **68**, 389-399 (2012).

76. E. Heiberg *et al.*, Design and validation of Segment--freely available software for cardiovascular image analysis. *BMC Med Imaging* **10**, 1 (2010).

77. D. Paganin, S. C. Mayo, T. E. Gureyev, P. R. Miller, S. W. Wilkins, Simultaneous phase and amplitude extraction from a single defocused image of a homogeneous object. *Journal of Microscopy* **206**, 33-40 (2002).

78. P. M. Rothwell, R. J. Gibson, J. Slattery, R. J. Sellar, C. P. Warlow, Equivalence of measurements of carotid stenosis. A comparison of three methods on 1001 angiograms. European Carotid Surgery Trialists' Collaborative Group. *Stroke; a journal of cerebral circulation* **25**, 2435-2439 (1994).

79. P. M. Rothwell, S. A. Gutnikov, C. P. Warlow, Reanalysis of the final results of the European Carotid Surgery Trial. *Stroke; a journal of cerebral circulation* **34**, 514-523 (2003).

80. M. Eliasziw *et al.*, Significance of plaque ulceration in symptomatic patients with high-grade carotid stenosis. North American Symptomatic Carotid Endarterectomy Trial. *Stroke; a journal of cerebral circulation* **25**, 304-308 (1994).

81. H. J. Barnett *et al.*, Benefit of carotid endarterectomy in patients with symptomatic moderate or severe stenosis. North American Symptomatic Carotid Endarterectomy Trial Collaborators. *The New England journal of medicine* **339**, 1415-1425 (1998).

82. J. L. Saver, CLINICAL PRACTICE. Cryptogenic Stroke. *The New England journal of medicine* **374**, 2065-2074 (2016).

83. S. S. Virani *et al.*, Heart Disease and Stroke Statistics-2020 Update: A Report From the American Heart Association. *Circulation* **141**, e139-e596 (2020).

84. B. A. Wasserman, R. J. Wityk, H. H. Trout, 3rd, R. Virmani, Low-grade carotid stenosis: looking beyond the lumen with MRI. *Stroke; a journal of cerebral circulation* **36**, 2504-2513 (2005).

85. A. Saxena, E. Y. K. Ng, S. T. Lim, Imaging modalities to diagnose carotid artery stenosis: progress and prospect. *Biomed Eng Online* **18**, 66-66 (2019).

86. B. C. Campbell, P. J. Mitchell, Endovascular therapy for ischemic stroke. *The New England journal of medicine* **372**, 2365-2366 (2015).

87. M. Goyal *et al.*, Randomized assessment of rapid endovascular treatment of ischemic stroke. *The New England journal of medicine* **372**, 1019-1030 (2015).

88. T. G. Jovin *et al.*, Thrombectomy within 8 hours after symptom onset in ischemic stroke. *The New England journal of medicine* **372**, 2296-2306 (2015).

89. J. L. Saver *et al.*, Stent-retriever thrombectomy after intravenous t-PA vs. t-PA alone in stroke. *The New England journal of medicine* **372**, 2285-2295 (2015).

90. L. Saba *et al.*, Carotid Artery Wall Imaging: Perspective and Guidelines from the ASNR Vessel Wall Imaging Study Group and Expert Consensus Recommendations of the American Society of Neuroradiology. *AJNR. American journal of neuroradiology* **39**, E9-e31 (2018).

91. G. D. Rubin, N. M. Rofsky, CT and MR Angiography : Comprehensive Vascular Assessment. (2015).

92. N. Cassola *et al.*, Duplex ultrasound for diagnosing symptomatic carotid stenosis in the extracranial segments. *Cochrane Database Syst Rev* **2018**, CD013172 (2018).

93. P. Libby, P. M. Ridker, G. K. Hansson, Progress and challenges in translating the biology of atherosclerosis. *Nature* **473**, 317-325 (2011).

94. C. Wang *et al.*, Quantitative Susceptibility Mapping for Characterization of Intraplaque Hemorrhage and Calcification in Carotid Atherosclerotic Disease. *Journal of magnetic resonance imaging : JMRI* 10.1002/jmri.27064 (2020).

95. A. Koops *et al.*, Multicontrast-weighted magnetic resonance imaging of atherosclerotic plaques at 3.0 and 1.5 Tesla: ex-vivo comparison with histopathologic correlation. *European radiology* **17**, 279-286 (2007).

96. W. K. Seo, K. Oh, S. I. Suh, H. Y. Seol, Clinical Significance of Wall Changes After Recanalization Therapy in Acute Stroke: High-Resolution Vessel Wall Imaging. *Stroke; a journal of cerebral circulation* **48**, 1077-1080 (2017).

97. A. Renú *et al.*, Vessel Wall Enhancement and Blood–Cerebrospinal Fluid Barrier Disruption After Mechanical Thrombectomy in Acute Ischemic Stroke. *Stroke; a journal of cerebral circulation* **48**, 651-657 (2017).

98. P. Abraham *et al.*, Vessel wall signal enhancement on 3-T MRI in acute stroke patients after stent retriever thrombectomy. *Neurosurgical focus* **42**, E20 (2017).

99. S. Power *et al.*, Vessel wall magnetic resonance imaging in acute ischemic stroke: effects of embolism and mechanical thrombectomy on the arterial wall. *Stroke; a journal of cerebral circulation* **45**, 2330-2334 (2014).

100. D. M. Mandell, M. Mossa-Basha, Intracranial Vessel Wall MRI: Principles and Expert Consensus Recommendations of the American Society of Neuroradiology. **38**, 218-229 (2017).

101. J. D. Bodle *et al.*, High-resolution magnetic resonance imaging: an emerging tool for evaluating intracranial arterial disease. *Stroke; a journal of cerebral circulation* **44**, 287-292 (2013).

102. O. Viessmann, L. Li, P. Benjamin, P. Jezzard, T2-Weighted intracranial vessel wall imaging at 7 Tesla using a DANTE-prepared variable flip angle turbo spin echo readout (DANTE-SPACE). *Magnetic resonance in medicine* **77**, 655-663 (2017).

Advanced Vascular Imaging

In this thesis, we used multiple methods to image pathological changes in the arterial wall of the middle cerebral artery and the carotid bifurcation, focusing on the carotid atherosclerotic plaque in stroke and TIA patients, either in vivo or ex vivo. The aim was to optimize contrast and image resolution to facilitate interpretation and comparison with histology. The methods we used were 3T, 7T, 11,7T MRI, and synchrotron-based phase-contrast μCT.

My Truong, M.D., is a senior consultant in Neuroradiology at Skåne University Hospital, Lund, Sweden.

FACULTY OF MEDICINE

LUND UNIVERSITY